Separation and Purification Technology 241 (2020) 116706

Contents lists available at ScienceDirect

Separation and Purification Technology

journal homepage: www.elsevier.com/locate/seppur

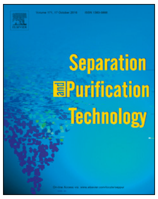

Using transient breakthrough experiments for screening of adsorbents for separation of C_2H_4/CO_2 mixtures

Ilona van Zandvoort[a], Erik-Jan Ras[a], Robbert de Graaf[a], Rajamani Krishna[b,*]

[a] Avantium Chemicals B.V., Zekeringstraat 29, 1014 BV Amsterdam, the Netherlands
[b] Van 't Hoff Institute for Molecular Sciences, University of Amsterdam, Science Park 904, 1098 XH Amsterdam, the Netherlands

ARTICLE INFO

Keywords:
Ethylene recovery
Oxidative coupling of methane
Biomass gasification
Transient breakthrough
Zeolites
Activated carbon
Mixture adsorption
Non-ideality
Selectivity reversal

ABSTRACT

The recovery of C_2H_4 from gaseous reactor effluents from processes such as oxidative coupling of methane (OCM), and biomass gasification (at relatively low temperatures (770–880 °C) is becoming of increasing industrial and economic importance. The reactor effluents are $N_2/H_2/CO/CO_2/CH_4/C_2H_6/C_2H_4$ mixtures, typically containing less than 15% C_2H_4. For recovery of C_2H_4, pressure swing adsorption (PSA) technology using a selective adsorbent offers an energy-efficient alternative to the more conventional separation schemes such as amine absorption and cryogenic distillation The major objective of this investigation is to screen commercially available cation exchanged zeolites (13X, CaX, NaY, 5A, 4A) and activated carbon (AC) to determine the most suitable adsorbent. For all these materials, the adsorption strengths of CO_2, and C_2H_4 are significantly higher than that of other gaseous constituents; consequently, the C_2H_4/CO_2 separation selectivity is the key to the efficacy of any adsorbent. The variety of adsorbents were screened using transient breakthrough experiments with feed mixtures using different C_2H_4/CO_2 ratios. On the basis of the breakthroughs, the adsorbents could be distinguished in three different categories: (i) 13X and 4A are selective to CO_2, (ii) CaX, NaY, and 5A are virtually non-selective, and (iii) AC is selective to C_2H_4 over the entire range of feed compositions and is therefore the adsorbent of choice.

The experimental breakthrough results are also compared with simulations using published unary isotherm data, along with the Ideal Adsorbed Solution Theory (IAST) for determination of mixture adsorption equilibrium. This comparison demonstrates that screening adsorbents solely on the basis of IAST calculations is likely to be misleading. This article underscores the need for performing transient breakthrough experiments with realistic feed gas mixtures for process modelling and development purposes.

1. Introduction

Ethene (C_2H_4, commonly referred to as ethylene) is a valuable petrochemical feedstock that is primarily produced on a large scale by naphtha cracking. Due to increasing demand and the desire to replace fossil fuels, alternative sources of C_2H_4 have received increased attention in recent years; two such alternatives are discussed below.

The oxidative coupling of methane (OCM) process involves reaction of CH_4 with oxygen under high temperatures (973–1173 K) to produce C_2H_6, followed by in-situ oxidation to C_2H_4 [1]. The partial or total combustion to CO or CO_2 are the main side reactions. Typically, the conversion of methane $< 40\%$ and the selectivity to C_2H_6 and to C_2H_4 is less than 50% and the reactor effluent consists of $H_2/CO/CO_2/CH_4/C_2H_6/C_2H_4$ mixtures typically containing $< 10\%$ C_2H_4. The conventional schemes for recovery of C_2H_4, involving amine absorption followed by cryogenic distillation at high pressure, are energy intensive [2,3]. Use of pressure swing adsorption (PSA) technology for C_2H_4 recovery offers the potential for development of an energy-efficient OCM process [1,4–6]. The optimal process scheme for implementation of PSA technology requires use of a C_2H_4-selective sorbent in which the C_2H_4-free raffinate is recycled back to the reaction train [5]; see Fig. 1. CO_2 is removed from the C_2H_4-rich extract stream and subsequently distilled to obtain C_2H_4 of the required purity. C_2H_6, the bottoms product from the distillation tower, is used as purge gas in the PSA section and recycled to the OCM reaction unit.

Biomass gasification at temperatures in the range 770–880 °C results in a syngas mixture, which also contains CO_2, C_2H_6, along with the valuable C_2H_4 in concentrations up to 16% [7]. Recovery of C_2H_4 by selective adsorption could significantly contribute to the economic viability of syngas production from biomass.

---

* Corresponding author.
E-mail address: r.krishna@contact.uva.nl (R. Krishna).

https://doi.org/10.1016/j.seppur.2020.116706
Received 10 October 2019; Received in revised form 9 February 2020; Accepted 11 February 2020

Nomenclature

Latin alphabet

A	surface area per kg of framework, m^2 kg^{-1}
c_i	molar concentration of species *i*, mol m^{-3}
c_{i0}	molar concentration of species *i* in fluid mixture at inlet, mol m^{-3}
c_t	total molar concentration of gas mixture, mol m^{-3}
C	constant used in Eq. (9), kg mol^{-1}
D_{ax}	axial dispersion coefficient, m^2 s^{-1}
$Đ_i$	Maxwell-Stefan diffusivity for molecule-wall interaction, m^2 s^{-1}
G^{excess}	excess Gibbs free energy, J mol^{-1}
L	length of packed bed adsorber, m
m_{ads}	mass of adsorbent in packed tube, kg
n	number of species in the mixture, dimensionless
N_i	molar flux of species *i* with respect to framework, mol m^{-2} s^{-1}
p_i	partial pressure of species *i*, Pa
p_t	total system pressure, Pa
P_i^0	sorption pressure, Pa
q_i	molar loading species *i*, mol kg^{-1}
Q	volumetric flow rate, m^3 s^{-1}
r	radial direction coordinate, m
r_c	radius of crystallite, m
R	gas constant, 8.314 J mol^{-1} K^{-1}
T	absolute temperature, K
v	interstitial gas velocity in packed bed, m s^{-1}
x_i	mole fraction of species *i* in adsorbed phase, dimensionless
y_i	mole fraction of species *i* in bulk fluid mixture, dimensionless
z	distance along the adsorber, m

Greek letters

γ_i	activity coefficient of component *i* in adsorbed phase, dimensionless
ε	voidage of packed bed, dimensionless
Λ_{ij}	Wilson parameters, dimensionless
π	spreading pressure, N m^{-1}
ρ	framework density, kg m^{-3}

Subscripts

i,j	components in mixture
T	referring to total mixture

Superscripts

0	referring to pure component loading
excess	referring to excess parameter

For most available adsorbents, CO_2, and C_2H_4 are more strongly adsorbed than H_2, CH_4, CO, and C_2H_6; consequently, the efficacy of any PSA scheme, such as that shown in Fig. 1, requires the sorbent to have a high C_2H_4/CO_2 separation selectivity. Bachman et al. [4] have recently reported that Mn_2(*m*-dobdc) (*m*-dobdc^{4-} = 4,6-dioxido-1,3-benzenedicarboxylate), a metal-organic framework (MOF) featuring a high density of unsaturated Mn^{2+} sites, offers a C_2H_4/CO_2 separation selectivity of about 10. In the context of the OCM process scheme (cf. Fig. 1), Bachman et al. [4] conclude "unique metal-adsorbate interactions facilitated by Mn_2(*m*-dobdc) render this material an outstanding adsorbent for the capture of ethylene from the product mixture, enabling this potentially disruptive alternative process for ethylene production".

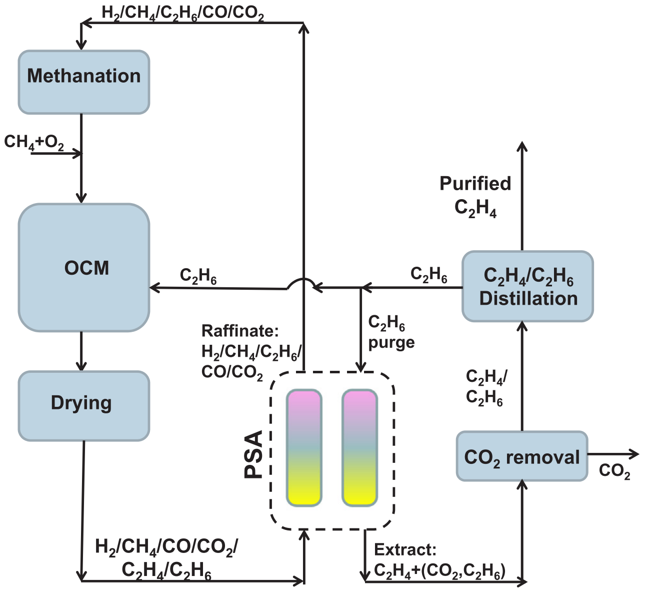

Fig. 1. OCM process flow scheme with C_2H_4-selective adsorbent in the PSA adsorber beds; this flow scheme is adapted from Radaelli et al. [5].

The primary objective of this article is examine whether any commercially available adsorbents could offer comparable C_2H_4/CO_2 separation (disruptive?) capabilities, obviating the need for development of novel MOFs. Prior to embarking on an extensive experimental campaign, we use literature data on unary isotherms, along with the Ideal Adsorbed Solution Theory (IAST) of Myers and Prausnitz [8] to compare the performance of Mn_2(*m*-dobdc) with different commercially available sorbents such as cation exchanged zeolites (13X, CaX, NaY, 5A, 4A) and activated carbon (AC). For this purpose, the required unary isotherm data are culled from literature sources; the isotherm data, along with the details of IAST methodology, are provided in the Supplementary material accompanying this publication. It must be noted that the unary isotherm data for CO_2, and C_2H_4 in AC, used in the IAST calculations are for heterogeneous microporous activated carbon (Type BPL, 6/16 mesh, manufactured by the Pittsburgh Chemical Company) as reported by Reich et al. [9].

Briefly, the basic equation of IAST is the analogue of Raoult's law for vapor-liquid equilibrium, i.e.

$$p_i = P_i^0 x_i; \quad i = 1, 2, \ldots n \tag{1}$$

where x_i is the mole fraction in the adsorbed phase

$$x_i = \frac{q_i}{q_1 + q_2 + \ldots q_n} \tag{2}$$

and P_i^0 is the pressure for sorption of every component *i*, which yields the same spreading pressure, π for each of the pure components, as that for the mixture:

$$\frac{\pi A}{RT} = \int_0^{P_1^0} \frac{q_1^0(f)}{f} df = \int_0^{P_2^0} \frac{q_2^0(f)}{f} df = \int_0^{P_3^0} \frac{q_3^0(f)}{f} df = \ldots \tag{3}$$

where $q_i^0(f)$ is the *pure* component adsorption isotherm, and f is the gas phase fugacity. The units of $\frac{\pi A}{RT}$ are mol kg^{-1} and is referred to as the adsorption potential [10], The adsorption potential can be determined by analytic integration of the unary isotherm data fits for each component. The total mixture loading is q_t is calculated from

$$q_t = q_1 + q_2 . ..+q_n = \frac{1}{\frac{x_1}{q_1^0(P_1^0)} + \frac{x_2}{q_2^0(P_2^0)} + ...+\frac{x_n}{q_n^0(P_n^0)}} \tag{4}$$

The entire set of Eqs. (1)–(4) need to be solved numerically to obtain the molar loadings, q_i of the individual components in the mixture.

In Fig. 2, the IAST calculations of the adsorbed phase mole fraction of C_2H_4 for binary $C_2H_4(1)/CO_2(2)$ mixtures, x_1, is plotted as a function of the mole fraction of C_2H_4 in the bulk gas phase mixture, y_1. The larger the departure from the parity line, $x_1 = y_1$, the more selective is adsorption from the mixture. The data for 5A, 4A, 13X, NaY, and CaX lie below the parity line, indicating that these materials preferentially adsorb CO_2. Zeolite 5A, the material with the largest deviation from the parity line, has the highest selectivity to CO_2, whereas the CO_2/C_2H_4 selectivity of CaX and NaY are close to unity. For selective adsorption of C_2H_4, the best performing material is Mn_2(*m*-dobdc), in agreement with the calculations in Bachman et al. [4] The IAST calculations for activated carbon (AC) also display selectivity towards C_2H_4.

In order to determine the reliability of IAST estimations for C_2H_4/CO_2 mixture adsorption, as shown in Fig. 2, transient breakthrough experiments were performed. The secondary objective of this article is to highlight some shortcomings of adopting a sorbent screening strategy relying only on IAST calculations of selectivities of mixture adsorption.

2. Transient breakthrough experiments

Transient breakthrough experiments were performed in a Flowrence set-up, described in earlier works [11,12], with multiple packed tubes (4 mm i.d., 300 mm height) that can be operated sequentially to test different sorbent materials for the same feed mixture under isothermal conditions; the experimental details are summarized in the Supplementary Material accompanying this publication. The sorbent beds are packed with six different commercial materials: 13X (Aldrich), CaX (Siliporite), NaY (CBV 100 CY, Zeolyst), 4A (=NaA = LTA-4A, Acros), 5A (=CaA = LTA-5A, Acros), and Activated carbon (GCN 3070 Cabot corp.), that were crushed and sieved to obtain 150–250 µm particles. At the start of each run, the materials are dried with flow of 25 N mL/min N_2 per tube at 473 K for 2 h. During the duration of the transient adsorption and desorption process, the packed bed is maintained under isothermal conditions at 313 K. The fixed-bed tube is first flushed, i.e. equilibrated, with pure N_2 at the specified total pressure, before injection of the feed mixture at time $t = 0$. The feed to each tube consists of $C_2H_4/CO_2/N_2/Ar$ mixtures using different C_2H_4/CO_2 ratios; N_2 forms about 58% and serves as diluent in order to maintain nearly constant flow conditions and reduce axial dispersion. About 2% Ar in the feed serves as inert internal tracer to monitor the start of the component breakthroughs. All the experiments reported in this article are conducted at 1 bar absolute pressure and 313 K.

For each sorbent, four different C_2H_4/CO_2 ratios in the feed mixture are chosen: Run 1 ($C_2H_4/CO_2 \approx 3$), Run 2 ($C_2H_4/CO_2 \approx 1.5$), Run 3 ($C_2H_4/CO_2 \approx 0.8$), and Run 4 ($C_2H_4/CO_2 \approx 0.5$). Figs. S6–S11 provide a summary of the experimental breakthroughs for each of the six sorbents. As illustration, Figs. 3 and 4 provide comparisons of the breakthroughs for Runs 1, and Run 4, respectively, for each sorbent. For 13X, CaX, NaY, 5A, and AC, the breakthrough characteristics are reasonably sharp, indicating that diffusional limitations are of negligible importance. It is worth noting that the breakthroughs of C_2H_4, and CO_2 occur at practically the same time for CaX, and NaY. For 4A zeolite, the breakthroughs have distended characteristics, indicative of intra-crystalline diffusional limitations. The breakthroughs with 5A are remarkable because in Run 1, C_2H_4 breaks through before CO_2, whereas in Run 4, CO_2 breaks through earlier than C_2H_4.

3. Numerical analysis of transient breakthrough experiments

First, we seek comparisons of the breakthrough experiments with the IAST calculations in Fig. 2 by constructing a x_1 vs y_1 diagram using the methodology in earlier works [13,14]. Let m_{ads} represent the mass of adsorbent, expressed in kg, packed into the tube that is fed with the feed mixture at a constant flow rate of Q m^3 s^{-1}. The uptake of C_2H_4, expressed as moles per kg of adsorbent in the packed tube, can be determined from a material balance

$$q_1 = \frac{c_t Q}{m_{ads}} \int_0^{t_{ss}} (y_{1,feed} - y_{1,exit})dt \tag{5}$$

In Eq. (5), c_t represents the total molar concentration of the entering feed mixture at 1 bar, and 313 K. The upper limit of the integral, t_{ss}, is the time required to reach steady-state. Analogously, the uptake of CO_2 is

$$q_2 = \frac{c_t Q}{m_{ads}} \int_0^{t_{ss}} (y_{2,feed} - y_{2,exit})dt \tag{6}$$

The integrals in Eqs. (5) and (6) can be numerically evaluated using a quadrature formula. In our analysis, we found that the use of the Simpson's rule provided results of good accuracy. Combining Eqs. (5) and (6) we can determine the mole fraction of C_2H_4, $x_1 = q_1/(q_1 + q_2)$, essentially invoking the assumption that the mixture can be considered to be a pseudo-binary due to the relatively poor adsorptivity of both Ar and N_2 present in the feed mixture. Fig. 5a presents the results of this foregoing numerical analysis in which the adsorbed phase mole fraction of C_2H_4, x_1, is plotted as a function of the mole fraction of C_2H_4 in the feed mixture, y_1, treated as a pseudo-binary.

In agreement with the IAST estimations in Fig. 2, the sorbents 4A, and 13X are CO_2-selective, and AC is C_2H_4-selective. The data for CaX, and NaY lie close to the $x_1 = y_1$ parity line in Fig. 5a; this indicates selectivities are close to unity for both these adsorbents. Indeed, examination of Figs. 3 and 4 show that the breakthroughs of C_2H_4, and CO_2 occur at practically the same time for CaX, and NaY.

In striking contrast to the expectations of the IAST estimates in Fig. 2, the data for 5A zeolite lie close to the parity line, indicating selectivities close to unity. Remarkably, 5A zeolite exhibits a tendency for selectivity reversal for $y_1 < 0.5$. Analogous selectivity reversals for 5A zeolite have been reported in the experiments reported by Calleja et al. [15] and Basmadjian and Hsieh [16]; see Figs. S19 and S20. The reasons for such selectivity reversal can be traced to the non-idealities in mixture adsorption, as detailed in earlier works [12,15,16]. Configurational Bias Monte-Carlo (CBMC) simulations for mixtures of CO_2-alkane mixtures in cation-exchanged zeolites reveal that the non-idealities are caused due to inhomogeneous distribution of guest molecules within the pore space, engendered by congregation of guest molecules around the extra-framework cations [17,18].

To account for non-ideality effects in mixture adsorption in 5A

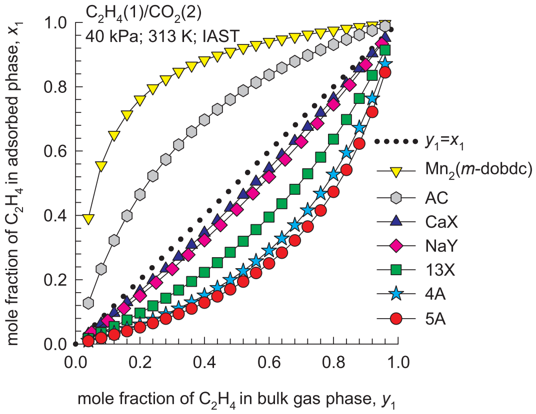

Fig. 2. IAST calculations for adsorption of binary $C_2H_4(1)/CO_2(2)$ mixtures in different sorbents at 313 K and total pressure of 1 bar. The adsorbed phase mole fraction of C_2H_4, x_1, is plotted as a function of the mole fraction of C_2H_4 in the bulk gas phase mixture, y_1. See Supplementary Material for information on the unary isotherm fit parameters and details of IAST calculations.

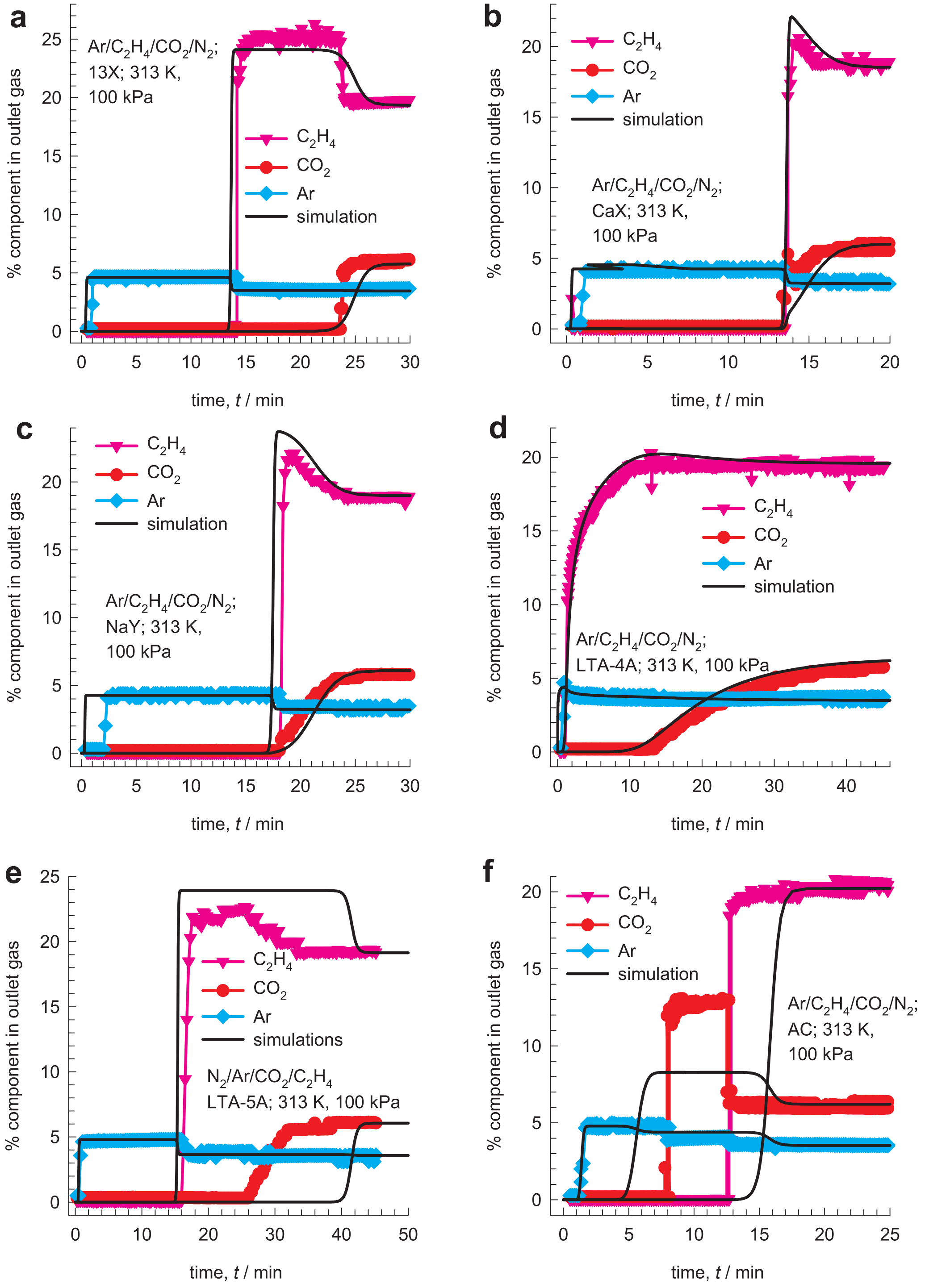

Fig. 3. Experimental breakthroughs for Ar/C_2H_4/CO_2/N_2 mixtures in (a) 13 X, (b) CaX, (c) NaY, (d) 4A, (e) 5A, and (f) AC. The total pressure is 1 bar, and temperature $T = 313$ K. The feed mixture composition corresponds to Run 1 (C_2H_4/CO_2 ≈ 3). The continuous solid black lines are breakthrough simulations using the IAST for determination of mixture adsorption equilibrium. The % N_2 in the outlet gas can be determined by the taking the sum of the mole % = 100.

zeolite, we need to introduce activity coefficients γ_i into Eq. (1)

$$p_i = P_i^0 x_i \gamma_i \tag{7}$$

The implementation of the activity coefficients is termed as the Real Adsorbed Solution Theory (RAST). Following the approaches of Myers, Talu, and Sieperstein [8,10,19,20] the excess Gibbs free energy for binary mixture adsorption is modeled as follows

$$\frac{G^{excess}}{RT} = x_1 \ln(\gamma_1) + x_2 \ln(\gamma_2) \tag{8}$$

The Wilson model for activity coefficients are given for binary mixtures by

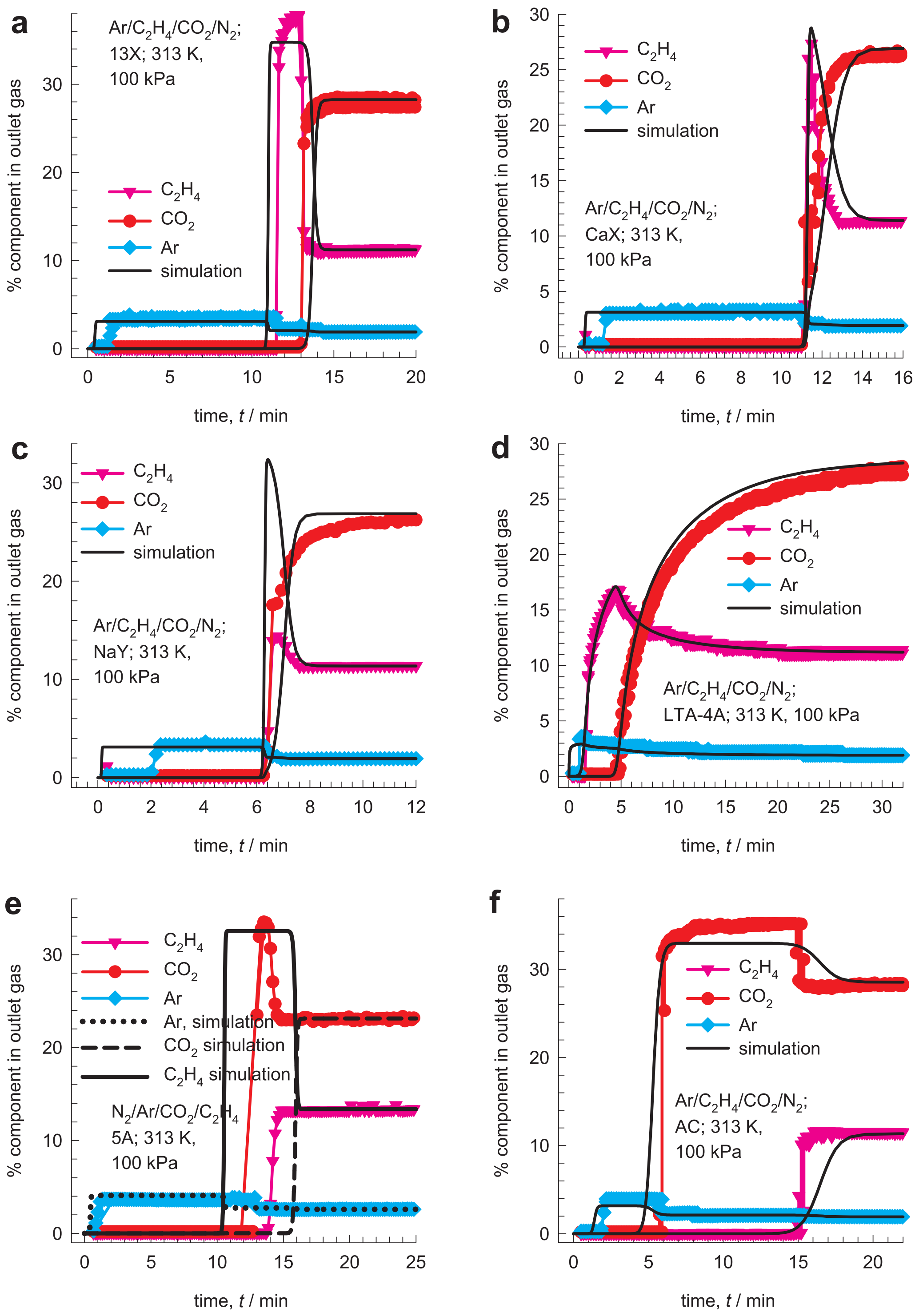

Fig. 4. Experimental breakthroughs for Ar/C$_2$H$_4$/CO$_2$/N$_2$ mixtures in (a) 13 X, (b) CaX, (c) NaY, (d) 4A, (e) 5A, and (f) AC. The total pressure is 1 bar, and temperature T = 313 K. The feed mixture composition corresponds to Run 4 (C$_2$H$_4$/CO$_2$ ≈ 0.5). The continuous solid black lines are breakthrough simulations using the IAST for determination of mixture adsorption equilibrium. The % N$_2$ in the outlet gas can be determined by the taking the sum of the mole % = 100.

$$\ln(\gamma_1) = \left(1 - \ln(x_1\Lambda_{11} + x_2\Lambda_{12}) - \frac{x_1\Lambda_{11}}{x_1\Lambda_{11} + x_2\Lambda_{12}} - \frac{x_2\Lambda_{21}}{x_2 + x_1\Lambda_{21}}\right)\left(1 - \exp\left(-C\frac{\pi A}{RT}\right)\right)$$
$$\ln(\gamma_2) = \left(1 - \ln(x_1\Lambda_{21} + x_2\Lambda_{22}) - \frac{x_1\Lambda_{12}}{x_1\Lambda_{11} + x_2\Lambda_{12}} - \frac{x_2\Lambda_{22}}{x_1\Lambda_{21} + x_2\Lambda_{22}}\right)\left(1 - \exp\left(-C\frac{\pi A}{RT}\right)\right) \quad (9)$$

In Eq. (9), $\Lambda_{11} = 1$; $\Lambda_{22} = 1$, and C is a constant with the units kg mol^{-1}. The introduction of $\left(1 - \exp\left(-C\frac{\pi A}{RT}\right)\right)$ imparts the correct limiting behaviors $\gamma_i \to 1$; $\frac{\pi A}{RT} \to 0$ for the activity coefficients in the Henry regime, $p_t \to 0$; $\frac{\pi A}{RT} \to 0$. As pore saturation conditions are approached, this correction factor tends to unity $\left(1 - \exp\left(-C\frac{\pi A}{RT}\right)\right) \to 1$. The choice of $\Lambda_{12} = \Lambda_{21} = 1$ in Eq. (9), yields unity values for the activity coefficients reduces to the IAST. The x_1 vs y_1

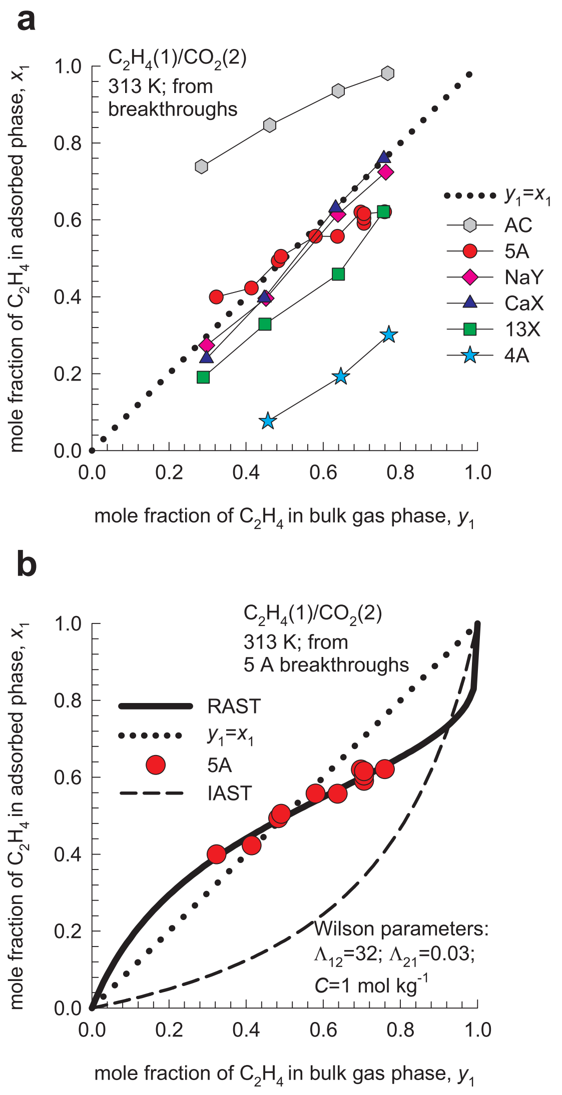

Fig. 5. (a) Analysis of the experimental breakthroughs with six different sorbents. The adsorbed phase mole fraction of C_2H_4, x_1, is plotted as a function of the mole fraction of C_2H_4 in the bulk gas phase mixture, y_1. (b) The experimental data x_1 vs y_1 for 5A zeolite, that includes the entire data set obtained at 1 bar and reported in earlier work [12], are compared with RAST calculations in which the fitted Wilson parameters $\Lambda_{12} = 32$; $\Lambda_{21} = 0.03$; $C = 1$ mol kg $^{-1}$ are used to describe the non-idealities for the C_2H_4/CO_2 binary pair.

data for 5A zeolite are well represented by the choice of the Wilson parameters $\Lambda_{12} = 32$; $\Lambda_{21} = 0.03$; $C = 1$ mol kg $^{-1}$ as evidenced by the RAST calculations represented by the solid black line in Fig. 5b.

4. Transient breakthrough simulations

Transient breakthroughs in fixed bed adsorbers are influenced by adsorption selectivities, uptake capacities, and intra-particle diffusional influences [21–24]. Therefore, we performed breakthrough simulations for direct comparison with the experimental breakthroughs. The use of more detailed process modelling of PSA operations, such as that described by Khalighi et al. [25], is beyond the scope of this work.

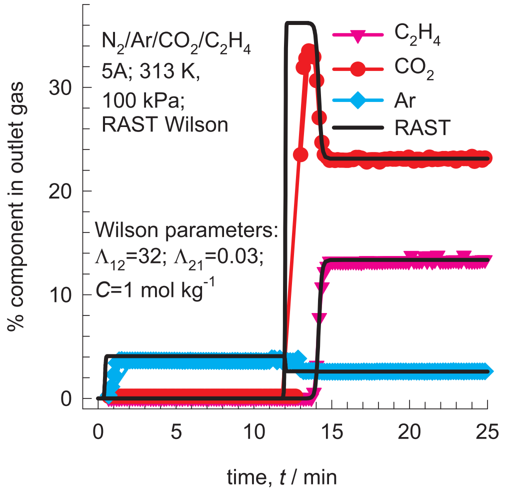

Fig. 6. Experimental breakthroughs for $Ar/C_2H_4/CO_2/N_2$ mixtures in 5A zeolite. The total pressure is 1 bar, temperature $T = 313$ K, and the feed mixture composition corresponds to Run 4 ($C_2H_4/CO_2 \approx 0.5$). The continuous solid black lines are breakthrough simulations using the RAST for determination of mixture adsorption equilibrium. In the RAST calculations, wherein the fitted Wilson parameters $\Lambda_{12} = 32$; $\Lambda_{21} = 0.03$; $C = 1$ mol kg $^{-1}$ are used to describe the non-idealities for the C_2H_4/CO_2 binary pair; all other pairs of guest molecules are assumed to behave ideally. The % N_2 in the outlet gas can be determined by the taking the sum of the mole % = 100.

For an n-component gas mixture flowing through a fixed bed adsorber maintained under isothermal, isobaric, conditions, the molar concentrations in the gas phase at any position and instant of time are obtained by solving the following set of partial differential equations for each of the species i in the gas mixture [21–24]

$$-D_{ax}\frac{\partial^2 c_i(t,z)}{\partial z^2}+\frac{\partial c_i(t,z)}{\partial t}+\frac{\partial(v(t,z)c_i(t,z))}{\partial z}+\frac{(1-\varepsilon)}{\varepsilon}\rho\frac{\partial \bar{q}_i(t,z)}{\partial t}=0;\quad i=1,2,\ldots n \tag{10}$$

In Eq. (10), t is the time, z is the distance along the adsorber, ε is the bed voidage, D_{ax} is the axial dispersion coefficient, v is the interstitial gas velocity, and $\bar{q}_i(t,z)$ is the *spatially averaged* molar loading within the crystallites of radius r_c, monitored at position z, and at time t [23]. Ruthven et al. [22] state "when mass transfer resistance is significantly greater than axial dispersion, one may neglect the axial dispersion term and assume plug flow". The assumption of plug flow is invoked in all the simulation results presented in this article.

The radial distribution of molar loadings, q_i, is obtained from a solution of a set of differential equations describing the transient uptake within a spherical crystallite of radius r_c

$$\rho\frac{\partial q_i(r,t)}{\partial t}=-\frac{1}{r^2}\frac{\partial}{\partial r}(r^2N_i) \tag{11}$$

The intra-crystalline fluxes N_i, in turn, are related to the radial gradients in the molar loadings by

$$N_i=-\rho Đ_i\frac{\partial q_i}{\partial r};\quad i=1,2\ldots n \tag{12}$$

In Eq. (12), $Đ_i$ is the Maxwell-Stefan (M-S) diffusivity for interaction of species i with the material framework. The use of Eq. (12) essentially implies that we are ignoring the influence of thermodynamic coupling effects [26].

At any time t, the component loadings at the surface of the particle $q_i(r_c,t)=q_i^*$ is in equilibrium with the bulk phase gas mixture; the loadings q_i^* are determined by use of the IAST, or RAST.

The spatial-averaged component loading within the crystallites of radius r_c is calculated using

$$\bar{q}_i(t)=\frac{3}{r_c^3}\int_0^{r_c}q_i(r,t)r^2dr \tag{13}$$

At time, $t = 0$, the inlet to the adsorber, $z = 0$, is subjected to a step input of the feed gas mixture, with inlet partial pressures p_{i0}, and this step input is maintained till the end of the adsorption cycle when steady-state conditions are reached.

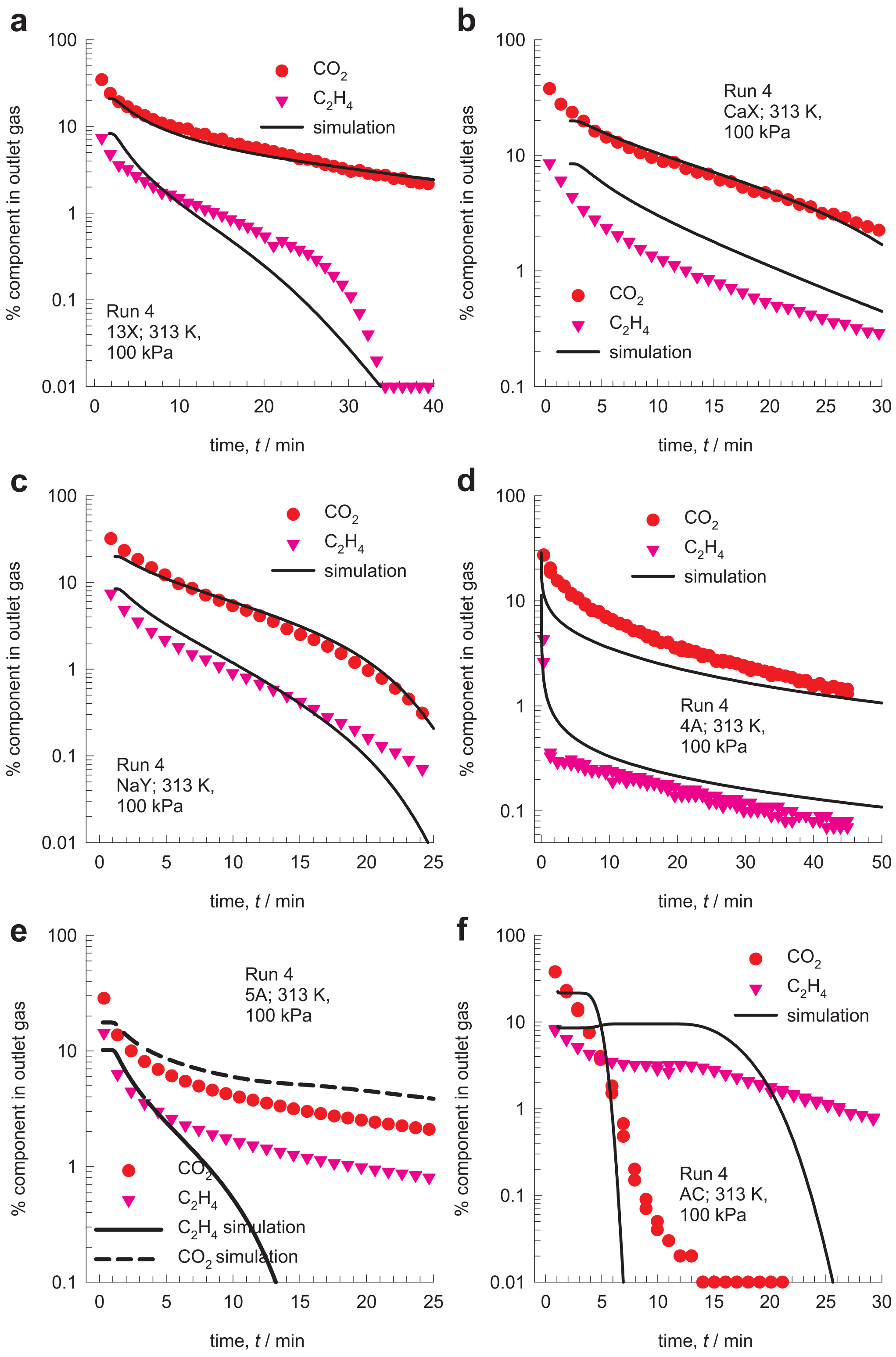

Fig. 7. Transient desorption data for the equilibrated bed in Run 4 for (a) 13 X, (b) CaX, (c) NaY, (d) 4A, (e) 5A, and (f) AC. The total pressure is 1 bar, and temperature $T = 313$ K. The continuous solid black lines are desorption simulations using the IAST for determination of mixture adsorption equilibrium. The % N_2 in the outlet gas can be determined by the taking the sum of the mole % = 100.

$$t \geqslant 0; \quad p_i(0, t) = p_{i0}; \quad c_i(0, t) = c_{i0} \tag{14}$$

Combination of the discretized partial differential equations along with the algebraic IAST equations describing mixture adsorption equilibrium results in a set of differential-algebraic equations, which are solved using a sparse matrix solver based on the semi-implicit Runge-Kutta method; further numerical details are provided in the Supplementary material.

To match the experiments with 4A zeolite, intra-crystalline diffusional influences must be accounted for in the breakthrough simulations. The best match was obtained by taking the values of $Đ_i/r_c^2 = 0.1\ \mathrm{s}^{-1}$ for Ar, N_2, and CO_2; For C_2H_4, the inter-cage hopping is significantly hindered by cations, and the choice $Đ_i/r_c^2 = 0.01 \text{ s}^{-1}$ yielded the best fits with experiments. For all other sorbents, intra-particle diffusional influences may be neglected. For Run 1, and Run 4, the continuous solid black lines in Figs. 3 and 4 represent the breakthrough simulations; more detailed comparisons for each of the four runs with different C_2H_4/CO_2 ratios are provided in Figs. S13–S18.

For 13X, CaX, and NaY zeolites, the breakthrough simulations show the correct qualitative features as the experimental data. However, the match is not quantitatively perfect; the simulations tend to predict a larger gap between the breakthrough times of C_2H_4 and CO_2. This indicates that the unary isotherms anticipate more CO_2-selective separations than is achieved in practice.

For 5A zeolite the agreement between experimental data and breakthrough simulations, based on the IAST, is poor; the selectivity reversal observed in Run 4 in favor of C_2H_4 is not anticipated by the breakthrough simulations. The selectivity reversal with 5A zeolite is also confirmed in the breakthrough experiments of García et al. [1] for 20/80 C_2H_4/CO_2 and 40/4/49/7 $CH_4/C_2H_6/CO_2/C_2H_4$ feed mixtures. In earlier work [12] it has been established that the non-idealities in mixture adsorption equilibrium are the root cause of selectivity reversals.

Fig. 6 shows that the transient breakthrough simulations incorporating the RAST is able to quantitatively capture the selectivity reversal phenomena for Run 4 with 5A zeolite. In the RAST implementation, the thermodynamic non-idealities are characterized by the Wilson parameters $\Lambda_{12} = 32$; $\Lambda_{21} = 0.03$; $C = 1 \text{ mol kg}^{-1}$, determined from fitting the x_1 vs y_1 data for 5A zeolite in Fig. 5b.

For AC, the transient breakthrough simulations show the same qualitative features as the experimental data but the quantitative match is poor because unary isotherm data used in the simulations were based on the literature data for microporous activated carbon (Type BPL, 6/16 mesh, manufactured by the Pittsburgh Chemical Company) and the experiments were performed with Cabot carbon.

5. Transient desorption: Experiments and simulations

For AC, the sorbent of choice, C_2H_4 is recovered in nearly purified form from extract phase of the PSA unit. To demonstrate the feasibility of this recovery, transient desorption experiments were conducted for each of the four runs 1, 2, 3, and 4. In the desorption experiments, the equilibrated bed is flushed with a constant flow of pure N_2, and the product compositions monitored by GC analysis. For the sake of completeness, desorption experiments were conducted for all six sorbents, not just for AC; the entire set of desorption experiments are presented in Figs. S19–S24. As illustration, the data for desorption for the equilibrated Run 4 are indicated by the symbols in Fig. 7. The continuous solid lines in Fig. 7 are the simulations of the desorption transience using the IAST for calculations of mixture adsorption equilibrium; the match with the experiments with AC are poor, as expected, because the unary isotherms are not for the Cabot AC used in the experiments.

For 13X and 4A zeolites, the data in Fig. 7a, d show that purified CO_2 can be recovered during the later stages of the transient desorption process. The data in Fig. 7b, c reinforce the conclusion, drawn earlier, that both CaX and NaY are non-selective to either constituent; neither constituent is available in pure form at the exit of the desorption cycle.

The desorption data for 5A shows that despite the selectivity reversal in favor of C_2H_4 is observed in the adsorption cycle (cf. Fig. 4e), neither of the constituent can be recovered in pure form during the desorption cycle; see Fig. 7e. Evidently, the selectivity reversal in favor of C_2H_4 is not strong enough to enable pure C_2H_4 recovery as raffinate.

The data in Fig. 7f provide confirmation of the ability of AC to produce nearly pure C_2H_4 for later stages of the desorption, $t > 12$ min.

6. Conclusions

Transient breakthrough experiments with C_2H_4/CO_2 feed mixtures in fixed beds packed with six different sorbents 13X, CaX, NaY, 5A, 4A, and AC were carried out to determine the most suitable adsorbent for selective adsorption of C_2H_4. The results indicate that AC is the most suitable adsorbent for this purpose. Though AC exhibits a lower C_2H_4/CO_2 selectivity than the tailor-made Mn_2(*m*-dobdc), its commercial availability obviates the need for materials development. Remarkably, the suitability of AC for selective adsorption of C_2H_4 from CO_2-bearing mixtures has not been highlighted in the published literature [1,4,5]. Of the other sorbents 4A, and 13X are CO_2-selective, and suitable for CO_2 capture of refinery off-gases containing C2 hydrocarbons. The sorbents CaX, NaY, and 5A zeolites are unable to produce purified products in either the rafffinate (adsorption cycle) or extract (desorption cycle) phases The results obtained also indicate that sorbent screening strategies relying on IAST calculations of mixture adsorption equilibrium, based on literature data on isotherms may be misleading. For 13X, NaY, CaX, and 5A zeolites, the actual separations are poorer than anticipated in the IAST calculations in Fig. 2.

CRediT authorship contribution statement

Ilona van Zandvoort: Conceptualization, Data curation, Investigation, Validation, Methodology, Project administration, Supervision, Writing – review & editing. **Erik-Jan Ras:** Conceptualization, Data curation, Investigation, Methodology, Project administration, Supervision, Writing – review & editing. **Robbert de Graaf:** Funding acquisition, Project administration, Supervision, Writing – review & editing. **Rajamani Krishna:** Methodology, Formal analysis, Software, Writing – original draft.

Declaration of Competing Interest

The authors declare that they have no known competing financial interests or personal relationships that could have appeared to influence the work reported in this paper.

Acknowledgement

Rijksdienst voor Ondernemend Nederland (RVO), Netherlands, Topsector Energie is acknowledged for financial support under project code TEBE117010.

Appendix A. Supplementary material

Supplementary data to this article can be found online at https://doi.org/10.1016/j.seppur.2020.116706.

References

[1] L. García, Y.A. Poveda, G. Rodríguez, E. Esche, H.R. Godini, G. Wozny, J.-U. Repke, A. Orjuela, Adsorption separation of oxidative coupling of methane effluent gases. miniplant scale experiments and modeling, J. Nat. Gas Sci. Eng. 61 (2019) 106–118, https://doi.org/10.1016/j.jngse.2018.11.007.

[2] H.R. Godini, M. Azadi, A. Penteado, M. Khadivi, G. Wozny, J.-U. Repke, A multi-perspectives analysis of methaneoxidative coupling process based onminiplant-scale experimental data, Chem. Eng. Res. Des. 151 (2019) 56–59, https://doi.org/10.1016/j.cherd.2019.08.002.

[3] A.T. Penteado, M. Kim, H.R. Godini, E. Esche, J.-U. Repke, Techno-economic evaluation of a bbiogas-based oxidative coupling of methane process for ethylene production, Front. Chem. Sci. Eng. 12 (2018) 598–618, https://doi.org/10.1007/s11705-018-1752-5.

[4] J.E. Bachman, D.A. Reed, M.T. Kapelewski, G. Chachra, D. Jonnavittula, G. Radaelli, J.R. Long, Enabling alternative ethylene production through its selective adsorption in the metal–organic framework Mn2(m-dobdc), Energy Environ. Sci. 11 (2018) 2423–2431, https://doi.org/10.1039/c8ee01332b.

[5] G. Radaelli, G. Chachra, D. Jonnavittula, Low-Energy, Low-Cost Production of Ethylene by Low- Temperature Oxidative Coupling of Methane, U.S. DOE/EERE/Advanced Manufacturing Office (AMO), https://www.osti.gov/servlets/purl/

1414280.

[6] X.S. Nghiem, Ethylene Production by Oxidative Coupling of Methane: New Process Flow Diagram Based on Adsorptive Separation, Ph.D. Thesis Technischen Universität Berlin, Berlin, 2014.

[7] C.M. Van der Meijden, Development of the MILENA Gasification Technology for the Production of Bio-SNG, Eindhovent University of Technology, Eindhoven, 2010 Ph.D. Thesis, Ph.D. Dissertation.

[8] A.L. Myers, J.M. Prausnitz, Thermodynamics of mixed gas adsorption, AIChE J. 11 (1965) 121–130.

[9] R. Reich, W.T. Zlegler, K.A. Rogers, Adsorption of Methane, Ethane, and Ethylene Gases and Their Binary and Ternary Mixtures and Carbon Dioxide on Activated Carbon at 212–301 K and Pressures to 35 Atmospheres, Ind. Eng. Chem. Process Des. Dev. 19 (1980) 336–344.

[10] F.R. Siperstein, A.L. Myers, Mixed-gas adsorption, AIChE J. 47 (2001) 1141–1159.

[11] I. van Zandvoort, G.P.M. van Klink, E. de Jong, J.C. van der Waal, Selectivity and Stability of Zeolites [Ca]A and [Ag]A towards Ethylene Adsorption and Desorption from Complex Gas Mixtures, Microporous Mesoporous Mat. 263 (2018) 142–149.

[12] I. van Zandvoort, J.K. van der Waal, E.-J. Ras, R. de Graaf, R. Krishna, Highlighting non-idealities in C2H4/CO2 mixture adsorption in 5A zeolite, Sep. Purif. Technol. 227 (2019), https://doi.org/10.1016/j.seppur.2019.115730.

[13] H. Yu, X. Wang, C. Xu, D.-L. Chen, W. Zhu, R. Krishna, Utilizing transient breakthroughs for evaluating the potential of Kureha carbon for CO_2 capture, Chem. Eng. J. 269 (2015) 135–147.

[14] R. Krishna, Methodologies for evaluation of metal-organic frameworks in separation applications, RSC Adv. 5 (2015) 52269–52295.

[15] G. Calleja, J. Pau, P. Perez, J.A. Calles, Binary and Ternary Adsorption Equilibria at High Pressure on Molecular Sieves, in: L. M.D. (Ed.), Fundamentals of Adsorption FOA 1996, Vol. 356. The Kluwer International Series in Engineering and Computer Science, Boston, Massachusetts, 1996, pp. 147–154. https://doi.org/10.1007/978-1-4613-1375-5_17.

[16] D. Basmadjian, S.T. Hsieh, Isothermal column sorption of ethylene-carbon dioxide mixtures with azeotropic behaviour, Can. J. Chem. Eng. 58 (1980) 185–189, https://doi.org/10.1002/cjce.5450580208.

[17] R. Krishna, J.M. van Baten, R. Baur, Highlighting the origins and consequences of thermodynamic nonidealities in mixture separations using zeolites and metal-organic frameworks, Microporous Mesoporous Mater. 267 (2018) 274–292, https://doi.org/10.1016/j.micromeso.2018.03.013.

[18] R. Krishna, J.M. Van Baten, Investigating the non-idealities in adsorption of CO2-bearing mixtures in cation-exchanged zeolites, Sep. Purif. Technol. 206 (2018) 208–217, https://doi.org/10.1016/j.seppur.2018.06.009.

[19] O. Talu, A.L. Myers, Rigorous thermodynamic treatment of gas-adsorption, AIChE J. 34 (1988) 1887–1893.

[20] O. Talu, I. Zwiebel, Multicomponent adsorption equilibria of nonideal mixtures, AIChE J. 32 (1986) 1263–1276.

[21] D.M. Ruthven, Principles of Adsorption and Adsorption Processes, John Wiley, New York, 1984.

[22] D.M. Ruthven, S. Farooq, K.S. Knaebel, Pressure swing adsorption, VCH Publishers, New York, 1994.

[23] R. Krishna, The maxwell-stefan description of mixture diffusion in nanoporous crystalline materials, Microporous Mesoporous Mater. 185 (2014) 30–50.

[24] R. Krishna, A maxwell-stefan-glueckauf description of transient mixture uptake in microporous adsorbents, Sep. Purif. Technol. 191 (2018) 392–399, https://doi.org/10.1016/j.seppur.2017.09.057.

[25] M. Khalighi, I.A. Karimi, S. Farooq, Comparing SiCHA and 4A zeolite for propylene/propane separation using a surrogate-based simulation/optimization approach, Ind. Eng. Chem. Res. 53 (2014) 16973–16983.

[26] R. Krishna, Highlighting the influence of thermodynamic coupling on kinetic separations with microporous crystalline materials, ACS Omega 4 (2019) 3409–3419, https://doi.org/10.1021/acsomega.8b03480.

Supplementary Material

Using Transient Breakthrough Experiments for Screening of Adsorbents for Separation of C_2H_4/CO_2 Mixtures

Ilona van Zandvoort, Erik-Jan Ras, Robbert de Graaf
Avantium Chemicals B.V.
Zekeringstraat 29
1014 BV Amsterdam, The Netherlands

and

Rajamani Krishna*
Van ‘t Hoff Institute for Molecular Sciences
University of Amsterdam
Science Park 904
1098 XH Amsterdam, The Netherlands
email: r.krishna@contact.uva.nl

Table of Contents

1 Preamble 4

2 Unary Isotherms.. 5

2.1 Isotherm fits for LTA-5A zeolite 5

2.2 Isotherm fits for 13X zeolite 5

2.3 Isotherm fits for CaX zeolite.. 6

2.4 Isotherm fits for NaY zeolite 6

2.5 Isotherm fits for LTA-4A zeolite 7

2.6 Isotherm fits for Activated Carbon 7

2.7 Isotherm fits for Mn_2(*m*-dobdc) 8

2.8 List of Tables for Unary Isotherms 9

3 IAST calculations of mixture adsorption 16

3.1 Brief outline of theory... 16

3.2 IAST calculations for C_2H_4/CO_2 mixture adsorption equilibrium.......................... 18

3.3 List of Figures for IAST calculations of mixture adsorption 20

4 The Real Adsorbed Solution Theory (RAST) 21

5 Methodology for transient breakthrough simulations 24

5.1 List of Figures for Methodology for transient breakthrough simulations................. 27

6 Transient breakthrough experiments vs simulations 29

6.1 The Flowrence set-up for transient breakthrough experiments 29

6.2 Experimental breakthrough campaigns.. 30

6.3 Numerical analysis of experimental breakthroughs 31

6.4 Experimental breakthroughs versus simulations.. 32

6.5 List of Figures for Transient breakthrough experiments vs simulations 34

7 Non-idealities in C_2H_4/CO_2 mixture adsorption in 5A zeolite 49

7.1 Analysis of Calleja data for C_2H_4/CO_2 mixture adsorption in 5A zeolite 49

7.2 Analysis of Basmadjian and Hsieh data for C_2H_4/CO_2 mixture adsorption in 5A zeolite......... 49

7.3 List of Figures for Non-idealities in C2H4/CO2 mixture adsorption in 5A zeolite 51

8 Transient desorption: experiments vs simulations 53

8.1 List of Figures for Transient desorption: experiments vs simulations...................................... 54

9 Nomenclature 60

10 References 63

1 Preamble

This Supporting Information accompanying the article *Using Transient Breakthrough Experiments for Screening of Adsorbents for Separation of C_2H_4/CO_2 Mixtures* provides:

(a) Unary isotherm data sources, and fits for various sorbents

(b) Brief summary of the IAST and RAST for calculation of mixture adsorption equilibrium

(c) Methodology used for transient breakthroughs in fixed bed adsorbers

(d) Flowrence set-up, and experimental breakthrough comparisons

(e) Detailed comparisons of experimental breakthroughs with transient breakthrough simulations

For ease of reading, the Supplementary Material is written as a stand-alone document.

2 Unary Isotherms

2.1 Isotherm fits for LTA-5A zeolite

The unary isotherm data for C_2H_4 in LTA-5A zeolite as reported in Table 2 and Table 3 of Mofarahi and Salehi[1] at temperatures of 283 K, 303 K, and 323 K were fitted with the dual-site Langmuir model

$$q = q_{A,sat} \frac{b_A p}{1 + b_A p} + q_{B,sat} \frac{b_B p}{1 + b_B p} \tag{S1}$$

with T-dependent parameters b_A, and b_B

$$b_A = b_{A0} \exp\left(\frac{E_A}{RT}\right); \quad b_B = b_{B0} \exp\left(\frac{E_B}{RT}\right) \tag{S2}$$

The fitted parameter values are presented in Table S1.

The unary isotherm data for CO_2 in LTA-5A zeolite as reported in Table A1 of Mofarahi and Gholipour[2] at temperatures of 273 K, 283 K, 303 K, 323 K, and 343 K were fitted with the dual-site Langmuir model; the parameter fits are presented in Table S2.

The unary isotherm data for N_2 in LTA-5A zeolite, as reported in Table 3 and Table 4 of Bakhtyari and Mofarahi[3] at temperatures of 273 K, 283 K, 303 K, 323 K, and 343 K were fitted with excellent accuracy with the single-site Langmuir model

$$q = q_{sat} \frac{bp}{1 + bp}; \quad b = b_0 \exp\left(\frac{E}{RT}\right) \tag{S3}$$

The fitted parameter values are presented in Table S3.

In the breakthrough simulations, the isotherm fits for N_2 in LTA-5A zeolite were assumed to also hold for Ar.

2.2 Isotherm fits for 13X zeolite

The unary isotherm data for CO_2, and C_2H_4 in 13X (= NaX) zeolite at temperatures of 279 K, 293 K, and 308 K are reported in Table I of Costa et al.[4] Their experimental data were fitted with the dual-site

Langmuir model with *T*- dependent parameters, as described by eqs (S1), and (S2); the fit parameters are reported in Table S4.

The unary isotherm data for N_2 in 13 X zeolite at temperatures of 298 K, 308 K, and 323 K are reported in Table 3 of Cavenati et al.[5] Their experimental data were fitted with the dual-site Langmuir model with *T*-dependent parameters, as described by eqs (S1), and (S2); the fit parameters are reported in Table S5. The idea of using *T*-dependent isotherm fits is that extrapolation to 313 K can be done for IAST calculations of selectivities and breakthroughs.

In the breakthrough simulations, the isotherm fits for N_2 in 13X zeolite were assumed to also hold for Ar.

2.3 Isotherm fits for CaX zeolite

The unary isotherm fit parameters for CO_2, and C_2H_4 in CaX zeolite at temperatures of 298.15 K, 308.15 K, and 318.15 K are reported in Supplementary Tables 9, and 10 of Bachman et al.[6] Their fit parameters, however, do not seem to be consistentwith the raw experimental data at 298.15 plotted in Figure 2. Therefore, the unary fit parameters were refitted in order to match the raw experimental data. The re-fitted parameters, using the 1-site Langmuir model with *T*-dependent parameters; these are reported in Table S6.

In the breakthrough simulations, the isotherm fits for N_2 and Ar are assumed to be the same as for 13X zeolite.

2.4 Isotherm fits for NaY zeolite

The unary isotherm data for CO_2, and C_2H_4 in NaY zeolite at temperatures of 305 K, and 353 K are presented in Figure 2 of Choudhary et al.[7] These data were re-fitted using the 1-site Langmur model with *T*-dependent parameters; the fit parameters are reported in Table S7 The idea of using *T*-dependent isotherm fits is that interpolation to 313 K can be done for IAST calculations of selectivities and breakthroughs.

In the breakthrough simulations, the isotherm fits for N_2 and Ar are assumed to be the same as for 13X zeolite.

2.5 Isotherm fits for LTA-4A zeolite

The unary isotherm fit parameters for CO_2, and C_2H_4 in LTA-4A (=CaA) zeolite at temperatures of 293.15 K, and 323.15 K are reported in Table 4 of Romero-Pérez and Aguilar-Armenta.[8] Their tabulated data for CO_2 were re-fitted with the dual-site Langmuir model with *T*-dependent parameters, as described by eqs (S1), and (S2); the fit parameters are reported in Table S8.

For C_2H_4 , their data were re-fitted with the 1-site Langmuir model with *T*-dependent parameters:

$$q = q_{sat}\frac{bp^{\nu}}{1+bp^{\nu}}; \quad b = b_0 \exp\left(\frac{E}{RT}\right) \tag{S4}$$

The fit parameters are reported in Table S9.

In the breakthrough simulations, the isotherm fits for N_2 and Ar are assumed to be the same as for LTA-5A zeolite.

2.6 Isotherm fits for Activated Carbon

The unary isotherm data for CO_2, and C_2H_4 for heterogeneous microporous activated carbon (Type BPL, 6/16 mesh, manufactured by the Pittsburgh Chemical Company) are reported by Reich et al.[9] The reported data at temperatures of 212.72 K, 260.2 K, and 301.4 K, reported in their Table 1, were fitted with the dual-site Langmuir model with *T*-dependent parameters, as described by eqs (S1), and (S2); the fit parameters are reported in Table S10. The idea of using *T*-dependent isotherm fits is that extrapolation to 313 K can be done for IAST calculations of selectivities and breakthroughs.

The unary isotherm data for N_2, and Ar for cylindrical activated carbon supplied by Kuraray Chemical company (Coal-derived activated carbon; 2GA-H2J) by Park et al.[10] The reported data at temperatures of 293 K, 308 K, and 323 K, in their Tables 9 and 11, were fitted with the 1-site Langmuir model with *T*-dependent parameters; the fit parameters are reported in Table S10.

2.7 Isotherm fits for Mn_2(*m*-dobdc)

The unary isotherm fit parameters for CO_2, and C_2H_4 in Mn_2(*m*-dobdc) (*m*-dobdc^{4-} = 4,6-dioxido-1,3-benzenedicarboxylate) at temperatures of 298.15 K, 308.15 K, and 318.15 K are reported in Supplementary Tables 1, and 2 of Bachman et al.[6] These data were re-fitted with the dual-site Langmuir model with *T*- dependent parameters, as described by eqs (S1), and (S2); the fit parameters are reported in Table S11.

2.8 List of Tables for Unary Isotherms

Table S1. Dual-site Langmuir parameter fits for C_2H_4 in LTA-5A zeolite. These parameters are based on the unary isotherm data reported in Table 2 and Table 3 of Mofarahi and Salehi[1] at temperatures of 283 K, 303 K, and 323 K.

	Site A			Site B		
	$q_{A,sat}$ mol kg^{-1}	b_{A0} Pa^{-1}	E_A kJ mol^{-1}	$q_{B,sat}$ mol kg^{-1}	b_{B0} Pa^{-1}	E_B kJ mol^{-1}
C_2H_4	2.5	6.98E-08	19	0.75	4.18E-18	67

Table S2. Dual-site Langmuir parameter fits for CO_2 in LTA-5A zeolite. These parameters are based on the unary isotherm data reported in Table A1 of Mofarahi and Gholipour[2] at temperatures of 273 K, 283 K, 303 K, 323 K, and 343 K.

	Site A			Site B		
	$q_{A,sat}$ mol kg^{-1}	b_{A0} Pa^{-1}	E_A kJ mol^{-1}	$q_{B,sat}$ mol kg^{-1}	b_{B0} Pa^{-1}	E_B kJ mol^{-1}
CO_2	1.5	4.5E-10	23.5	2.5	2.99E-12	49

Unary Isotherms

Table S3. Single-site Langmuir parameter fits for N_2 in LTA-5A zeolite. These parameters are based on the unary isotherm data reported in Table 3 and Table 4 of Bakhtyari and Mofarahi[3] at temperatures of 273 K, 283 K, 303 K, 323 K, and 343 K.

	q_{sat} mol kg^{-1}	b_0 Pa^{-1}	E kJ mol^{-1}
N_2	2.5	1.68E-09	16.6

Unary Isotherms

Table S4. Dual-site Langmuir parameter fits for CO_2 and C_2H_4 in 13X zeolite. These parameters are based on the unary isotherm data at temperatures of 279 K, 293 K, and 308 K as reported in Table I of Costa et al.[4]

	Site A			Site B		
	$q_{A,sat}$ mol kg^{-1}	b_{A0} Pa^{-1}	E_A kJ mol^{-1}	$q_{B,sat}$ mol kg^{-1}	b_{B0} Pa^{-1}	E_B kJ mol^{-1}
CO_2	2.0	4.813E-08	23	2.5	1.129E-12	42
C_2H_4	1.35	3.403E-05	4.6	1.4	8.508E-17	70

Table S5. Dual-site Langmuir parameter fits for N_2 in 13X zeolite. These parameters are based on the unary isotherm data at temperatures of 298 K, 308 K, and 323 K as reported in Table 3 of Cavenati et al.[5]

	Site A			Site B		
	$q_{A,sat}$ mol kg^{-1}	b_{A0} Pa^{-1}	E_A kJ mol^{-1}	$q_{B,sat}$ mol kg^{-1}	b_{B0} Pa^{-1}	E_B kJ mol^{-1}
N_2	3.0	4.075E-09	13	6.0	4.681E-10	13

Unary Isotherms

Table S6. 1-site Langmuir parameter fits for CO_2 and C_2H_4 in CaX zeolite. These re-fitted parameters are based on the data of Bachman et al.[6]

	q_{sat} mol kg^{-1}	b_0 Pa^{-1}	E kJ mol^{-1}
CO_2	3.5	2.0E-08	22
C_2H_4	5.4	3.6E-09	25

Table S7. 1-site Langmuir parameter fits for CO_2 and C_2H_4 in NaY zeolite. These parameters are based on the unary isotherm data from Figure 2 of Choudhary et al.[7]

	q_{sat} mol kg^{-1}	b_0 Pa^{-1}	E kJ mol^{-1}
CO_2	6.3	6.36E-10	30
C_2H_4	4.6	4.967E-09	25.3

Table S8. Dual-site Langmuir parameter fits for CO_2 in LTA-4A zeolite. The *T*-dependent parameters were obtained by re-fitting the data reported in Table 4 of Romero-Pérez and Aguilar-Armenta.[8]

	Site A			Site B		
	$q_{A,sat}$ mol kg^{-1}	b_{A0} Pa^{-1}	E_A kJ mol^{-1}	$q_{B,sat}$ mol kg^{-1}	b_{B0} Pa^{-1}	E_B kJ mol^{-1}
CO_2	1.3	6.075E-12	40	2.0	6.722E-12	50

Table S9. 1-site Langmuir-Freundlich parameter fits for C_2H_4 in LTA-4A zeolite. The *T*-dependent parameters were obtained by re-fitting the data reported in Table 4 of Romero-Pérez and Aguilar-Armenta.[8]

$$q = q_{sat}\frac{bp^{\nu}}{1+bp^{\nu}}; \quad b = b_0 \exp\left(\frac{E}{RT}\right)$$

	q_{sat} mol kg^{-1}	b_0 $\mathrm{Pa}^{-\nu}$	E kJ mol^{-1}	ν dimensionless
C_2H_4	2.3	6.287E-11	35	1.26

Table S10. Dual-site Langmuir parameter fits for CO_2 and C_2H_4 in Activated Carbon (BPL), obtained by fitting of the experimental data of Reich et al.[9] Single-site Langmuir parameter fits for N_2 and Ar in Activated Carbon (Kuraray), obtained by fitting of the experimental data of Park et al.[10]

	Site A			Site B		
	$q_{A,sat}$ mol kg^{-1}	b_{A0} Pa^{-1}	E_A kJ mol^{-1}	$q_{B,sat}$ mol kg^{-1}	b_{B0} Pa^{-1}	E_B kJ mol^{-1}
CO_2	3.5	5.617E-10	22.5	7.6	5.893E-11	22.6
C_2H_4	3.6	1.299E-09	24	4.4	9.630E-11	21.5
N_2	3.2	1.768E-09	16.5			
Ar	4.35	1.681E-09	15.2			

Table S11. Dual-site Langmuir parameter fits for CO_2, and C_2H_4 in Mn_2(*m*-dobdc), obtained by re-fitting of the data reported in Supplementary Tables 1, and 2 of Bachman et al.[6]

	Site A			Site B		
	$q_{A,sat}$ mol kg^{-1}	b_{A0} Pa^{-1}	E_A kJ mol^{-1}	$q_{B,sat}$ mol kg^{-1}	b_{B0} Pa^{-1}	E_B kJ mol^{-1}
CO_2	13.4	2.031E-11	27	6.2	7.627E-11	34
C_2H_4	2.45	3.435E-11	47	4.0	1.619E-11	42

3 IAST calculations of mixture adsorption

3.1 Brief outline of theory

Within microporous crystalline materials, the guest molecules exist in the adsorbed phase. The Gibbs adsorption equation[11] in differential form is

$$Ad\pi = \sum_{i=1}^{n} q_i d\mu_i \tag{S5}$$

The quantity A is the surface area per kg of framework, with units of m^2 per kg of the framework of the crystalline material; q_i is the molar loading of component i in the adsorbed phase with units moles per kg of framework; μ_i is the molar chemical potential of component i. The spreading pressure π has the same units as surface tension, i.e. N m^{-1}.

The chemical potential of any component in the adsorbed phase, μ_i, equals that in the bulk fluid phase. If the partial fugacities in the bulk fluid phase are f_i, we have

$$d\mu_i = RTd\ln f_i \tag{S6}$$

where R is the gas constant (= 8.314 J mol^{-1} K^{-1}).

Briefly, the basic equation of Ideal Adsorbed Solution Theory (IAST) theory of Myers and Prausnitz[12] is the analogue of Raoult's law for vapor-liquid equilibrium, i.e.

$$f_i = P_i^0 x_i; \quad i = 1,2,...n \tag{S7}$$

where x_i is the mole fraction in the adsorbed phase

$$x_i = \frac{q_i}{q_1 + q_2 + ...q_n} \tag{S8}$$

and P_i^0 is the pressure for sorption of every component i, which yields the same spreading pressure, π for each of the pure components, as that for the mixture:

IAST calculations of mixture adsorption

$$\frac{\pi A}{RT}=\int_0^{P_1^0}\frac{q_1^0(f)}{f}df=\int_0^{P_2^0}\frac{q_2^0(f)}{f}df=\int_0^{P_3^0}\frac{q_3^0(f)}{f}df=... \tag{S9}$$

where $q_i^0(f)$ is the *pure* component adsorption isotherm. The units of $\frac{\pi A}{RT}$, also called the adsorption potential,[13] are mol kg^{-1}.

The unary isotherm may be described by say the 1-site Langmuir isotherm

$$q^0(f)=q_{sat}\frac{bf}{1+bf};\quad \theta=\frac{bf}{1+bf} \tag{S10}$$

where we define the fractional *occupancy* of the adsorbate molecules, $\theta=q^0(f)/q_{sat}$. The superscript 0 is used to emphasize that $q^0(f)$ relates the *pure component* loading to the bulk fluid fugacity. More generally, the unary isotherms may need to be described by, say, the dual-site Langmuir model

$$q^0(f)=q_{A,sat}\frac{b_Af}{1+b_Af}+q_{B,sat}\frac{b_Bf}{1+b_B} \tag{S11}$$

Each of the integrals in Equation (S9) can be evaluated analytically:

$$\begin{aligned}\int_{f=0}^{P_i^0}\frac{q^0(f)}{f}df&=q_{A,sat}\ln\left(1+b_A\left(P_i^0\right)\right)+q_{B,sat}\ln\left(1+b_B\left(P_i^0\right)\right)\\ \int_{f=0}^{P_i^0}\frac{q^0(f)}{f}df&=q_{A,sat}\ln\left(1+b_A\left(\frac{f_i}{x_i}\right)\right)+q_{B,sat}\ln\left(1+b_B\left(\frac{f_i}{x_i}\right)\right)\end{aligned} \tag{S12}$$

The right hand side of equation (S12) is a function of P_i^0. For multicomponent mixture adsorption, each of the equalities on the right hand side of Equation (S9) must be satisfied. These constraints may be solved using a suitable equation solver, to yield the set of values of P_1^0, P_2^0, P_3^0,.. P_n^0, all of which satisfy Equation (S9). The corresponding values of the integrals using these as upper limits of integration must yield the same value of $\frac{\pi A}{RT}$ for each component; this ensures that the obtained solution is the correct one.

The adsorbed phase mole fractions x_i are then determined from

$$x_i = \frac{f_i}{P_i^0}; \quad i = 1,2,...n \tag{S13}$$

A key assumption of the IAST is that the enthalpies and surface areas of the adsorbed molecules do not change upon mixing. If the total mixture loading is q_t, the area covered by the adsorbed mixture is $\frac{A}{q_t}$ with units of m^2 (mol mixture)$^{-1}$. Therefore, the assumption of no surface area change due to mixture adsorption translates as $\frac{A}{q_t} = \frac{Ax_1}{q_1^0(P_1^0)} + \frac{Ax_2}{q_2^0(P_2^0)} + \cdots \frac{Ax_n}{q_n^0(P_n^0)}$; the total mixture loading is q_t is calculated from

$$q_t = q_1 + q_2 ... + q_n = \frac{1}{\frac{x_1}{q_1^0(P_1^0)} + \frac{x_2}{q_2^0(P_2^0)} + ... + \frac{x_n}{q_n^0(P_n^0)}} \tag{S14}$$

in which $q_1^0(P_1^0)$, $q_2^0(P_2^0)$,... $q_n^0(P_n^0)$ are determined from the unary isotherm fits, using the sorption pressures for each component P_1^0, P_2^0, P_3^0,.. P_n^0 that are available from the solutions to equations Equations (S9), and (S12).

The entire set of equations (S7) to (S14) need to be solved numerically to obtain the loadings, q_i of the individual components in the mixture.

3.2 IAST calculations for C_2H_4/CO_2 mixture adsorption equilibrium

In order to gauge the potential of different adsorbents for separating C_2H_4(1)/CO_2(2) mixtures we use the IAST calculations. Figure S1a presents IAST calculations for adsorption of binary C_2H_4(1)/CO_2(2) mixtures in different sorbents at 313 K and total pressure of 40 kPa, wherein the adsorbed phase mole fraction of C_2H_4 (*y*-axis) is plotted as a function of the mole fraction of C_2H_4 in the bulk gas phase mixture (*x*-axis). The dotted line represents the parity line, indicating no selective separation potential. The larger the departure from the $x_1 = y_1$, parity line, the more selective is mixture adsorption. Figure S1b presents calculations for the adsorption selectivity, S_ads, defined by

IAST calculations of mixture adsorption

$$S_{ads} = \frac{q_1/q_2}{y_1/y_2} \tag{S15}$$

where q_1 and q_2 are the molar loadings of the components 1, and 2 in the adsorbed phase in equilibrium with a bulk gas phase mixture with mole fractions y_1 and y_2.

The data for 5A, 4A, 13X, NaY, and CaX lie below the $x_1 = y_1$ parity line, indicating that these materials preferentially adsorb CO_2. LTA-5A, the material with the largest deviation from the $x_1 = y_1$ parity line, has the highest selectivity to CO_2. The data for CaX, and NaY lie very near the $x_1 = y_1$ parity line, and the preferential selectivity toward CO_2 is only marginal. For selective adsorption of C_2H_4, the best performing material is Mn_2(*m*-dobdc), as was also claimed in the paper by Bachman et al.[6] The IAST calculations for activated carbon (AC) also displays selectivity towards C_2H_4.

In order to determine the reliability of IAST predictions for C_2H_4/CO_2 mixture adsorption, we resort to transient breakthrough experiments, buttressed by transient breakthrough simulations incorporating the IAST.

3.3 List of Figures for IAST calculations of mixture adsorption

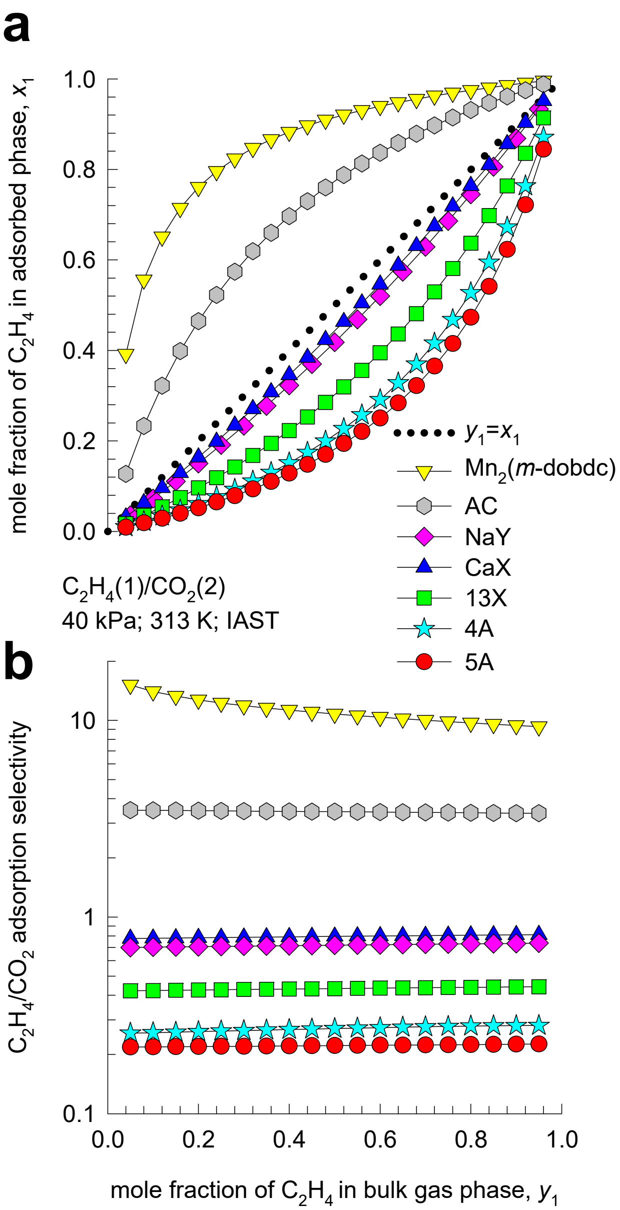

Figure S1. IAST calculations for adsorption of binary $C_2H_4(1)/CO_2(2)$ mixtures in different sorbents at 313 K and total pressure of 40 kPa. (a) The adsorbed phase mole fraction of C_2H_4, x_1, is plotted as a function of the mole fraction of C_2H_4 in the bulk gas phase mixture, y_1. (b) $C_2H_4(1)/CO_2(2)$ adsorption selectivity is plotted as a function of the y_1.

4 The Real Adsorbed Solution Theory (RAST)

To account for non-ideality effects in mixture adsorption, we introduce activity coefficients γ_i into Equation (S7) [12]

$$f_i = P_i^0 x_i \gamma_i \tag{S16}$$

Following the approaches of Myers, Talu, and Sieperstein[13-15] we model the excess Gibbs free energy for binary mixture adsorption as follows

$$\frac{G^{excess}}{RT} = x_1 \ln(\gamma_1) + x_2 \ln(\gamma_2) \tag{S17}$$

The Wilson model for activity coefficients are given for binary mixtures by

$$\begin{aligned}
\ln(\gamma_1) &= \left(1 - \ln(x_1\Lambda_{11} + x_2\Lambda_{12}) - \frac{x_1\Lambda_{11}}{x_1\Lambda_{11} + x_2\Lambda_{12}} - \frac{x_2\Lambda_{21}}{x_2 + x_1\Lambda_{21}}\right)\left(1 - \exp\left(-C\frac{\pi A}{RT}\right)\right) \\
\ln(\gamma_2) &= \left(1 - \ln(x_1\Lambda_{21} + x_2\Lambda_{22}) - \frac{x_1\Lambda_{12}}{x_1\Lambda_{11} + x_2\Lambda_{12}} - \frac{x_2\Lambda_{22}}{x_1\Lambda_{21} + x_2\Lambda_{22}}\right)\left(1 - \exp\left(-C\frac{\pi A}{RT}\right)\right)
\end{aligned} \tag{S18}$$

In Equation (S18), $\Lambda_{11} \equiv 1; \quad \Lambda_{22} \equiv 1$, and C is a constant with the units kg mol^{-1}. The introduction of $\left(1 - \exp\left(-C\frac{\pi A}{RT}\right)\right)$ imparts the correct limiting behaviors $\gamma_i \to 1; \quad \frac{\pi A}{RT} \to 0$ for the activity coefficients in the Henry regime, $f_t \to 0; \quad \frac{\pi A}{RT} \to 0$. As pore saturation conditions are approached, this correction factor tends to unity $\left(1 - \exp\left(-C\frac{\pi A}{RT}\right)\right) \to 1$. The choice of $\Lambda_{12} = \Lambda_{21} = 1$ in Equation (S18), yields unity values for the activity coefficients.

The excess reciprocal loading for the mixture can be defined as

$$\left(\frac{1}{q_t}\right)^{excess} = \frac{1}{q_t} - \left(\frac{x_1}{q_1^0(P_1^0)} + \frac{x_2}{q_2^0(P_2^0)}\right) \tag{S19}$$

The excess reciprocal loading for the mixture can be related to the partial derivative of the Gibbs free energy with respect to the adsorption potential at constant composition

The Real Adsorbed Solution Theory (RAST)

$$\left(\frac{1}{q_t}\right)^{excess} = \left.\frac{\partial\left(\frac{G^{excess}}{RT}\right)}{\partial\left(\frac{\pi A}{RT}\right)}\right|_{T,x} = \left[-x_1 \ln(x_1 + x_2\Lambda_{12}) - x_2 \ln\left(x_2 + x_1\Lambda_{21}\right)\right] C \exp\left(-C\frac{\pi A}{RT}\right) \tag{S20}$$

For calculation of the total mixture loading we need to replace Equation (S14) by

$$q_t \equiv q_1 + q_2 = \frac{1}{\frac{x_1}{q_1^0(P_1^0)} + \frac{x_2}{q_2^0(P_2^0)} + \left[-x_1 \ln(x_1 + x_2\Lambda_{12}) - x_2 \ln\left(x_2 + x_1\Lambda_{21}\right)\right] C \exp\left(-C\frac{\pi A}{RT}\right)} \tag{S21}$$

The parameters Λ_{12}, Λ_{21}, and C can be fitted to match the experimental data on mixture adsorption. The implementation of the activity coefficients is termed as the Real Adsorbed Solution Theory (RAST).

The Real Adsorbed Solution Theory (RAST)

5 Methodology for transient breakthrough simulations

We describe below the simulation methodology used to perform transient breakthrough calculations for fixed bed adsorbers (see schematics in Figure S2, and Figure S3). The simulation methodology is the same as used in our earlier publications.[16-19] For an *n*-component gas mixture flowing through a fixed bed maintained under isothermal, isobaric, conditions, the molar concentrations in the gas phase at any position and instant of time are obtained by solving the following set of partial differential equations for each of the species *i* in the gas mixture[18, 20-22]

$$-D_{ax}\frac{\partial^2 c_i(t,z)}{\partial z^2}+\frac{\partial c_i(t,z)}{\partial t}+\frac{\partial\left(v(t,z)c_i(t,z)\right)}{\partial z}+\frac{\left(1-\varepsilon\right)}{\varepsilon}\rho\frac{\partial \overline{q}_i(t,z)}{\partial t}=0;\quad i=1,2,...n \tag{S22}$$

In equation (S22), t is the time, z is the distance along the adsorber, ρ is the framework density, ε is the bed voidage, D_{ax} is the axial dispersion coefficient, v is the interstitial gas velocity, and $\overline{q}_i(t,z)$ is the *spatially averaged* molar loading within the crystallites of radius r_c, monitored at position z, and at time t. The time $t = 0$, corresponds to the time at which the feed mixture is injected at the inlet to the fixed bed. Prior to injection of the feed mixture, N_2 gas flows through the fixed bed. In this model described by equation (S22), the effects of all mechanisms that contribute to axial mixing are lumped into a single effect axial dispersion coefficient D_{ax}. Ruthven et al.[22] state that more detailed models that include radial dispersion are generally not necessary. They also make the following remark "when mass transfer resistance is significantly greater than axial dispersion, one may neglect the axial dispersion term and assume plug flow". All of the analysis and breakthrough simulations were carried out using the plug flow assumption.

The radial distribution of molar loadings, q_i, within a spherical crystallite, of radius r_c, is obtained from a solution of a set of differential equations describing the uptake

$$\rho\frac{\partial q_i(r,t)}{\partial t}=-\frac{1}{r^2}\frac{\partial}{\partial r}\left(r^2 N_i\right) \tag{S23}$$

The intra-crystalline fluxes N_i, in turn, are related to the radial gradients in the molar loadings by

$$N_i = -\rho Đ_i \frac{\partial q_i}{\partial r}; \quad i = 1, 2, \ldots\ldots n \tag{S24}$$

In eq (S23) $Đ_i$ is the Maxwell-Stefan (M-S) diffusivity for interaction of species *i* with the material framework.

For all times $t \geq 0$, the exterior of the crystal is brought into contact with a bulk gas mixture at partial pressures p_{i0} that is maintained constant till the crystal reaches thermodynamic equilibrium with the surrounding gas mixture. At any time *t*, the component loadings at the surface of the particle $q_i(r_c, t) = q_i^*$ is in equilibrium with the bulk phase gas mixture with partial pressures p_{i0}. In the general case, the component loadings are calculated using the Ideal Adsorbed Solution Theory (IAST) of Myers and Prausnitz.[12]

At any time *t*, during the transient approach to thermodynamic equilibrium, the spatial-averaged component loading within the crystallites of radius r_c is calculated using

$$\overline{q}_i(t) = \frac{3}{r_c^3} \int_0^{r_c} q_i(r,t) r^2 dr \tag{S25}$$

Summing equation (S25) over all *n* species in the mixture allows calculation of the *total average* molar loading of the mixture within the crystallite

$$\overline{q}_t(t,z) = \sum_{i=1}^{n} \overline{q}_i(t,z) \tag{S26}$$

The term $\frac{\partial \overline{q}_i(t,z)}{\partial t}$ in equation (S22) is determined by solving the set of equations (S23), and (S25), and (S26). At any time *t*, and position *z*, the component loadings at the outer surface of the particle $q_i(r_c, t, z)$ is in equilibrium with the bulk phase gas mixture with partial pressures $p_i(t,z)$ in the bulk gas mixture. In the general case, the component loadings $q_i(r_c, t, z)$ are calculated using the Ideal Adsorbed Solution Theory (IAST) of Myers and Prausnitz.[12]

Methodology for transient breakthrough simulations

If the value of $\frac{Đ_i}{r_c^2}$ is large enough to ensure that intra-crystalline gradients are absent and the entire crystallite particle can be considered to be in thermodynamic equilibrium with the surrounding bulk gas phase at that time *t*, and position *z* of the adsorber

$$\overline{q}_i(t,z) = q_i(t,z) \tag{S27}$$

The *interstitial* gas velocity is related to the *superficial* gas velocity by

$$v = \frac{u}{\varepsilon} \tag{S28}$$

At time, $t = 0$, the inlet to the adsorber, $z = 0$, is subjected to a step input of the *n*-component gas mixture and this step input is maintained till the end of the adsorption cycle when steady-state conditions are reached.

$$t \geq 0; \quad p_i(0,t) = p_{i0}; \quad u(0,t) = u_0 \tag{S29}$$

where $u_0 = v_0 \varepsilon$ is the superficial gas velocity at the inlet to the adsorber.

Typically, the adsorber length is divided into 100 slices, and each spherical crystallite was discretized into 20 equi-volume slices. The results thus obtained were confirmed to be of adequate accuracy. Combination of the discretized partial differential equations (PDEs) along with the algebraic equations describing mixture adsorption equilibrium (IAST, or mixed-gas Langmuir model, as appropriate), results in a set of differential-algebraic equations (DAEs), which are solved using BESIRK.[23] BESIRK is a sparse matrix solver, based on the semi-implicit Runge-Kutta method originally developed by Michelsen,[24] and extended with the Bulirsch-Stoer extrapolation method.[25] Use of BESIRK improves the numerical solution efficiency in solving the set of DAEs. The evaluation of the sparse Jacobian required in the numerical algorithm is largely based on analytic expressions.[20] Further details of the numerical procedures used in this work, are provided by Krishna and co-workers;[20, 21, 26, 27] interested readers are referred to our website that contains the numerical details.[21]

5.1 List of Figures for Methodology for transient breakthrough simulations

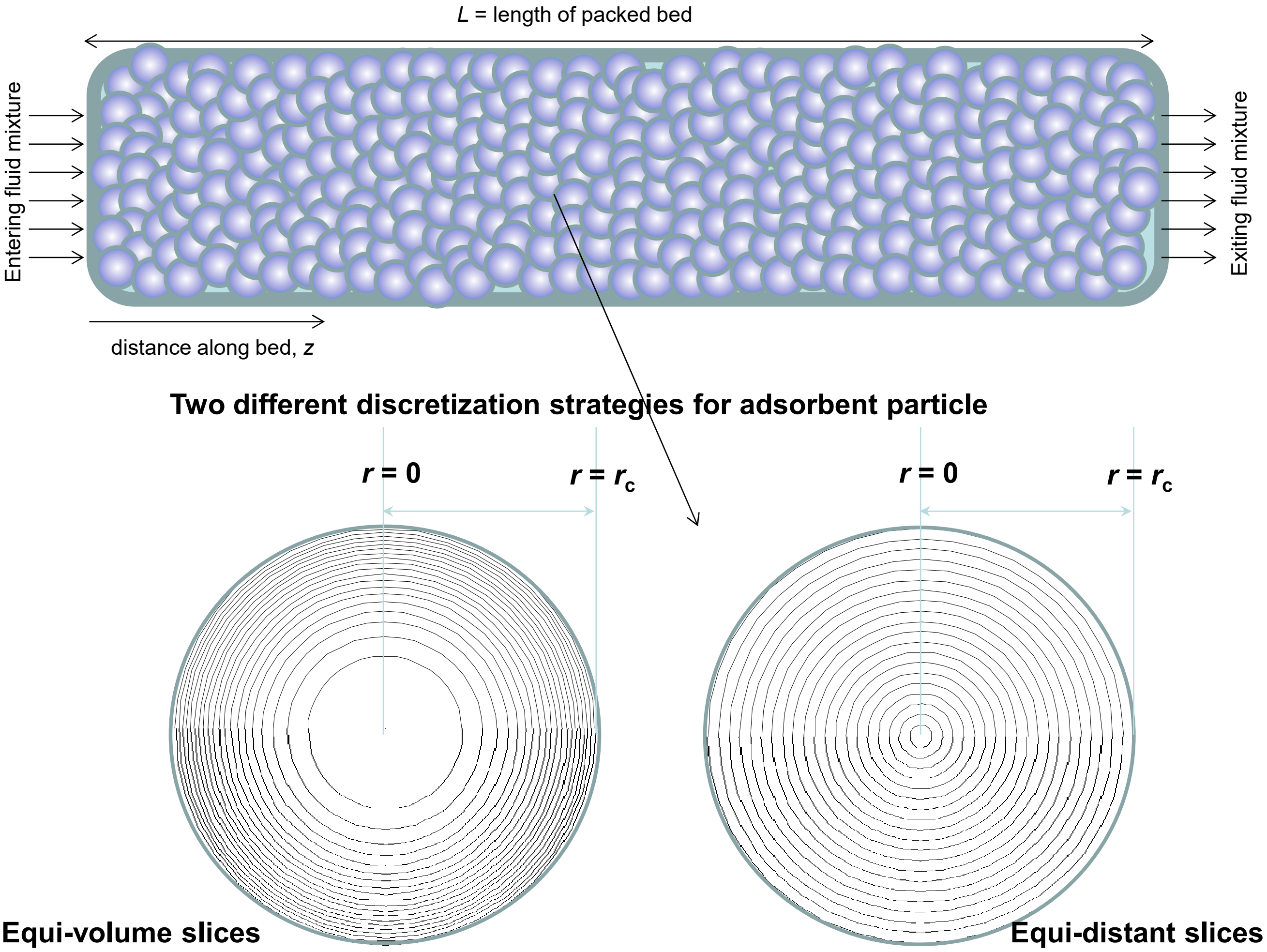

Figure S2. Two different discretization schemes for a single spherical crystallite.

Methodology for transient breakthrough simulations

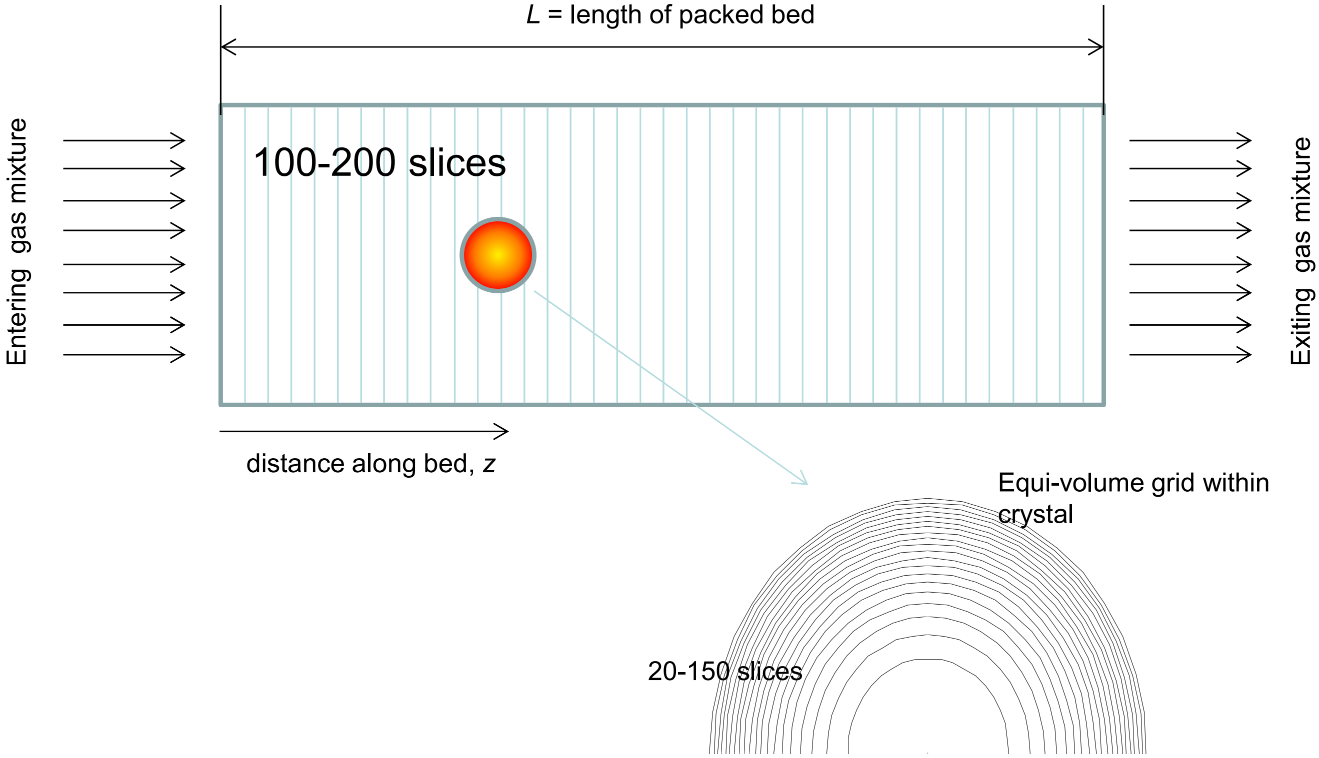

Figure S3. Discretization scheme for fixed bed adsorber.

6 Transient breakthrough experiments vs simulations

6.1 The Flowrence set-up for transient breakthrough experiments

A Flowrence set-up is modified for the transient breakthrough experiments (Figure S4) such that the feed selector valve selects one reactor (= fixed-bed adsorber) tube, which is fed with the adsorption gas mixture. Meanwhile, all other reactors are fed with nitrogen (the desorption gas). A selector valve in the effluent is used to lead the effluent gas from the selected reactor to the mass spectrometer (Hiden Analytical HPR-20 QIC). The selected reactor is fed with the mixed gas feed and continuously monitored by the MS (10 s interval).[28] A second selector valve is used to analyze the gas stream from one of the desorbing reactors (under N_2 flow) with a compact GC (Interscience), which is equipped with TCD and FID detectors to detect CO_2 and C_2H_4, respectively.

The Flowrence has four heated reactor blocks (40 - 300 °C), each containing four packed tubes of 560 mm height, 6 mm OD and 4 mm ID that can be pressurized (0-10 barg). The isothermal zone was determined to be 350 mm. During a run, one blank and 15 sorbent materials can be tested. At the bottom of the reactor a diluent gas (N_2) can be mixed with the effluent, which is used to dilute the gas flow before analysis, increase the flow rate and reduce the axial dispersion effects. At the start of each run, the materials are dried in the reactor under 25 NmL/min N_2 per reactor at 473 K for 2 h. All the experiments reported here were conducted at 1 bar absolute pressure, and 313 K. See also the schematic in Figure S5.

The sorbent bed is 4 mm in diameter, and 30 cm height. The sorbent beds are packed with commercial materials: 13X (Aldrich), [Na]A (=LTA-4A = 4A, Acros), [Ca]A (=LTA-5A = 5A, Acros), [Ca]X (Siliporite), NaY (CBV 100 CY, Zeolyst), and Activated carbon (GCN 3070 Cabot Corp.), that were crushed and sieved to obtain 150-250 μm particles.

A layer of SiC (inert diluent, particle size of 150 μm) was loaded in the reactors first to make sure that the sorbent bed is located in the isothermal zone. SiC is also used to fill up the interstitial void space between adsorbent particles and top of the reactors up to a height of 55 cm.

Transient breakthrough experiments vs simulations

A lecture bottle (Messer) containing 30 vol% C_2H_4, 5 vol % Ar and 65 vol% N_2 was used to determine C_2H_4 adsorption. CO_2 was mixed with the gas feed via a separate mass flow controller and the total feed flow was kept at 25 mL/min per reactor.

The fixed-bed tube is first flushed with pure N_2 at the specified total pressure, before injection of the feed mixture, at time $t = 0$. Ar is used as an inert internal standard to monitor the start of the adsorption experiment and calculate gas concentrations. In the desorption experiments, the equilibrated bed is flushed with a constant flow of pure N_2, and the product compositions monitored by GC analysis.

In the MS, ions are produced by electron ionization (EI), separated by a quadrupole analyzer and detected by a secondary electron multiplier (SEM). The raw signal was monitored at the selected m/z values, corrected for spectral overlap by taking into account the relative abundancies of the different peaks. The data was subsequently normalized to the signal of N_2 (relative sensitivity = 1). The selected m/z values and their relative sensitivities (RS) were calibrated using known concentrations of the gases. The percentage of each component is calculated based on the total normalized response. It should be noted that the molecular ion peaks of N_2, and C_2H_4 are observed at m/z 28. Therefore, m/z 27 was used to monitor the C_2H_4 concentration in the effluent gas.

6.2 Experimental breakthrough campaigns

The feed to each tube consists of $C_2H_4/CO_2/N_2/Ar$ mixtures using different C_2H_4/CO_2 ratios; N_2 forms about 58%, and Ar about 2%. Argon serves as inert internal tracer to signal the start of the component breakthroughs; N_2 serves as diluent in order to maintain nearly constant flow conditions and reduce axial dispersion. All the experiments reported here are conducted at 1 bar absolute pressure, and 313 K. The sorbents tried were cation-exchanged zeolites (13X, CaX, NaY, 4A, 5A) and activated carbon (from Cabot Corp.). All of the experiments were conducted at a temperature of 313 K and 1 bar operating pressure. Initially, the fixed bed was equilibrated by flow of pure N_2. At time $t = 0$, the packed tube was fed with $C_2H_4/CO_2/Ar/N_2$ mixtures of varying C_2H_4/CO_2 ratios. For each sorbent, four different C_2H_4/CO_2 ratios in the feed mixture were chosen: Run 1 ($C_2H_4/CO_2 \approx 3$), Run 2 ($C_2H_4/CO_2 \approx 1.5$), Run

3 ($C_2H_4/CO_2 \approx 0.8$), and Run 4 ($C_2H_4/CO_2 \approx 0.5$). The experimental results for the different sorbents are presented in Figure S6 (13X), Figure S7 (CaX), Figure S8 (NaY) , Figure S9 (LTA-4A), Figure S10 (LTA-5A), and Figure S11 (AC). In each of these Figures, the data for Runs 1, 2, 3 and 4 are indicated, respectively, by a, b, c, d. In all the experimental campaigns, steady-state conditions are established at the end of each experimental campaign. It is noteworthy that the breakthroughs obtained with LTA-4A display distended characteristics, indicative of strong intra-crystalline diffusion limitations. For all other sorbents, the breakthroughs obtained are sharp, indicating that intra-particle diffusion limitations are of negligible importance.

6.3 Numerical analysis of experimental breakthroughs

We first undertake a simple numerical analysis of the experimental breakthroughs in order to compare with the IAST calculations presented in Figure S1, using the methodology in earlier works.[17, 29] A brief outline of the analysis is presented below.

Let m_{ads} represent the mass of adsorbent, expressed in kg, packed into the tube that is fed with the C_2H_4(1)/CO_2(2) feed mixture at a constant flow rate of Q m^3 s^{-1}. The uptake of C_2H_4, expressed as moles per kg of adsorbent in the packed tube, can be determined from a material balance

$$q_1 = \frac{c_t Q}{m_{ads}} \int_0^{t_{ss}} \left(y_{1,feed} - y_{1,exit} \right) dt \tag{S30}$$

In eq (S30), c_t represents the total molar concentration of the entering feed mixture at 1 bar, and 313 K. The upper limit of the integral, t_{ss}, is the time required to reach stead-state. Analogously, the uptake of CO_2 is

$$q_2 = \frac{c_t Q}{m_{ads}} \int_0^{t_{ss}} \left(y_{2,feed} - y_{2,exit} \right) dt \tag{S31}$$

The integrals in eqs (S30), and (S31) can be determined numerical using a quadrature formula. In our analysis, we found that the use of the Simpson's rule provided results of good accuracy. Combining eqs (S30), and (S31) we can determine the mole fraction of C_2H_4, $x_1 = q_1/(q_1 + q_2)$, essentially invoking the assumption that the mixture can be considered to be a pseudo-binary due to the poor adsorptivity of bothAr and N_2 present in the feed mixture. Figure S12 presents the results of this foregoing numerical analysis in which the adsorbed phase mole fraction of C_2H_4 (*y*-axis), x_1, is plotted as a function of the mole fraction of C_2H_4 in the feed mixture, y_1, treated as a pseudo-binary.

Comparison with the IAST calculations presented in Figure S1, a number of observations emerge. Firstly, in agreement with the IAST predictions, the sorbents LTA-4A, and 13X are CO_2-selective. The data for CaX, and NaY zeolites show that both these adsorbents are practically non-selective to either component as the data lie close to the $y = x$ parity. Indeed, examination of Figure S7 (CaX), and Figure S8 (NaY) show that the breakthroughs of C_2H_4, and CO_2 occur at practically the same time. Contrary to the expectations of the IAST, 5A exhibits a tendency for selectivity reversal for $y_1 < 0.5$; the reasons for such selectivity reversal can be traced to the non-idealities in mixture adsorption, as detailed in earlier work.[30]

The most important conclusion to emerge is that AC is a suitable sorbent for selective adsorption of C_2H_4 from CO_2-bearing mixtures.

6.4 Experimental breakthroughs versus simulations

Transient breakthrough simulations were performed in order to compare with the experimental breakthroughs. In all the breakthrough simulations reported in this article, the IAST was used to model mixture adsorption equilibrium. The breakthroughs obtained with 4A have distended characteristics. To match the experiments, intra-crystalline diffusional influences must be accounted for in the breakthrough simulations. The best match was obtained by taking the values of $Đ_i/r_c^2$ = 0.1 s^{-1} for Ar, N_2, and CO_2; For C_2H_4, the intra-cage hopping is more hindered by cations, and the value $Đ_i/r_c^2$ = 0.01 s^{-1} yielded the best fits. Figure S13 compares the breakthrough experiments with simulations for the complete set of four runs; the match is very good.

Transient breakthrough experiments vs simulations

For 13X, CaX, NaY, 5A, and AC, the breakthrough characteristics are sharp, and intra-crystalline diffusional limitations are of negligible importance. The comparisons of the breakthrough experiments with simulations are presented in Figure S14, Figure S15, Figure S16, Figure S17, and Figure S18.

For 13X zeolite, the breakthrough simulations show the correct qualitative features as the experimental data; see Figure S14. However, the match is not quantitatively perfect. The simulations tend to predict a larger gap between the breakthrough times of C_2H_4 and CO_2; this indicates that the unary isotherms anticipate more selective separations than is achieved in practice.

For CaX, and NaY zeolites (see Figure S15, and Figure S16), tthe breakthrough simulations show the right qualitative trends as the experimental data, the gap between the breakthrough times of C_2H_4 and CO_2 is slightly larger than observed experimentally. Indeed, the experiments, show that C_2H_4 and CO_2 breakthrough at nearly the same time. The unary isotherm data, along with IAST, for CaX and NaY anticipate a somewhat higher CO_2/C_2H_4 selectivity than is realized in practice.

For 5A zeolite (see Figure S17), the agreement between experimental data and breakthrough simulations is significantly worse, the selectivity reversal observed in Run 5 is not anticipated by the breakthrough simulations using IAST for calculations of the mixture adsorption equilibrium. In earlier work[30] it has been established that the non-idealities in mixture adsorption equilibrium is the root cause of selectivity reversals.

For AC, the transient breakthrough simulations show the same qualitative features as the experimental data but the quantitative match is poor because unary isotherm data used in the simulations were based on the literature data for microporous activated carbon (Type BPL, 6/16 mesh, manufactured by the Pittsburgh Chemical Company).

6.5 List of Figures for Transient breakthrough experiments vs simulations

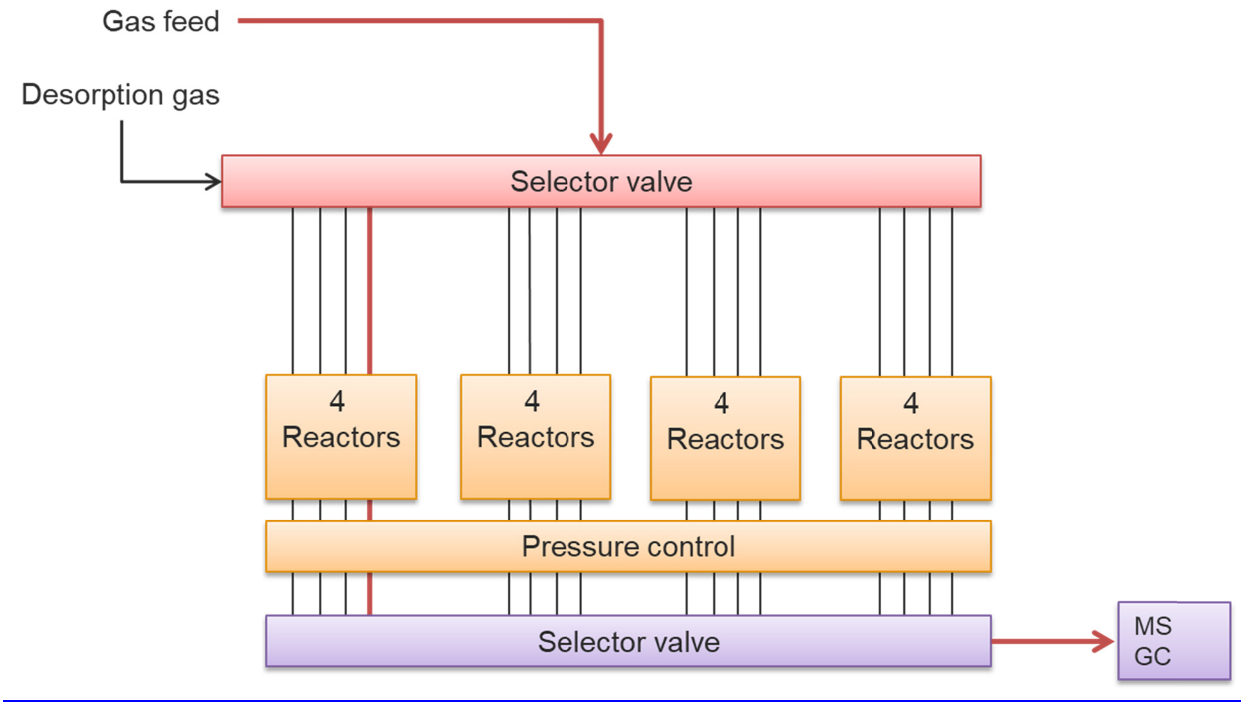

Figure S4. Schematic of experimental set up for transient breakthroughs.

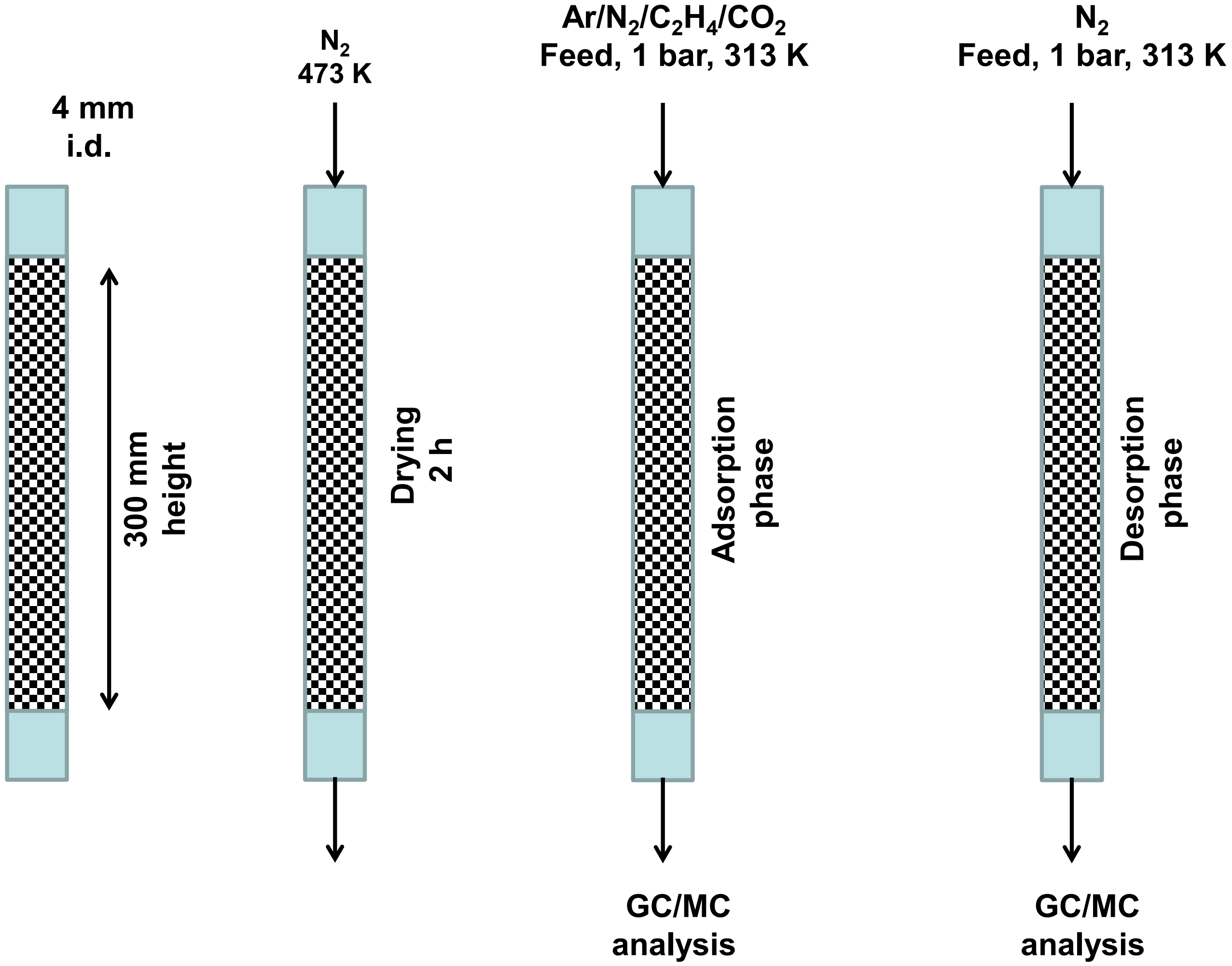

Figure S5. Schematic of experimental procedure for transient breakthroughs.

Transient breakthrough experiments vs simulations

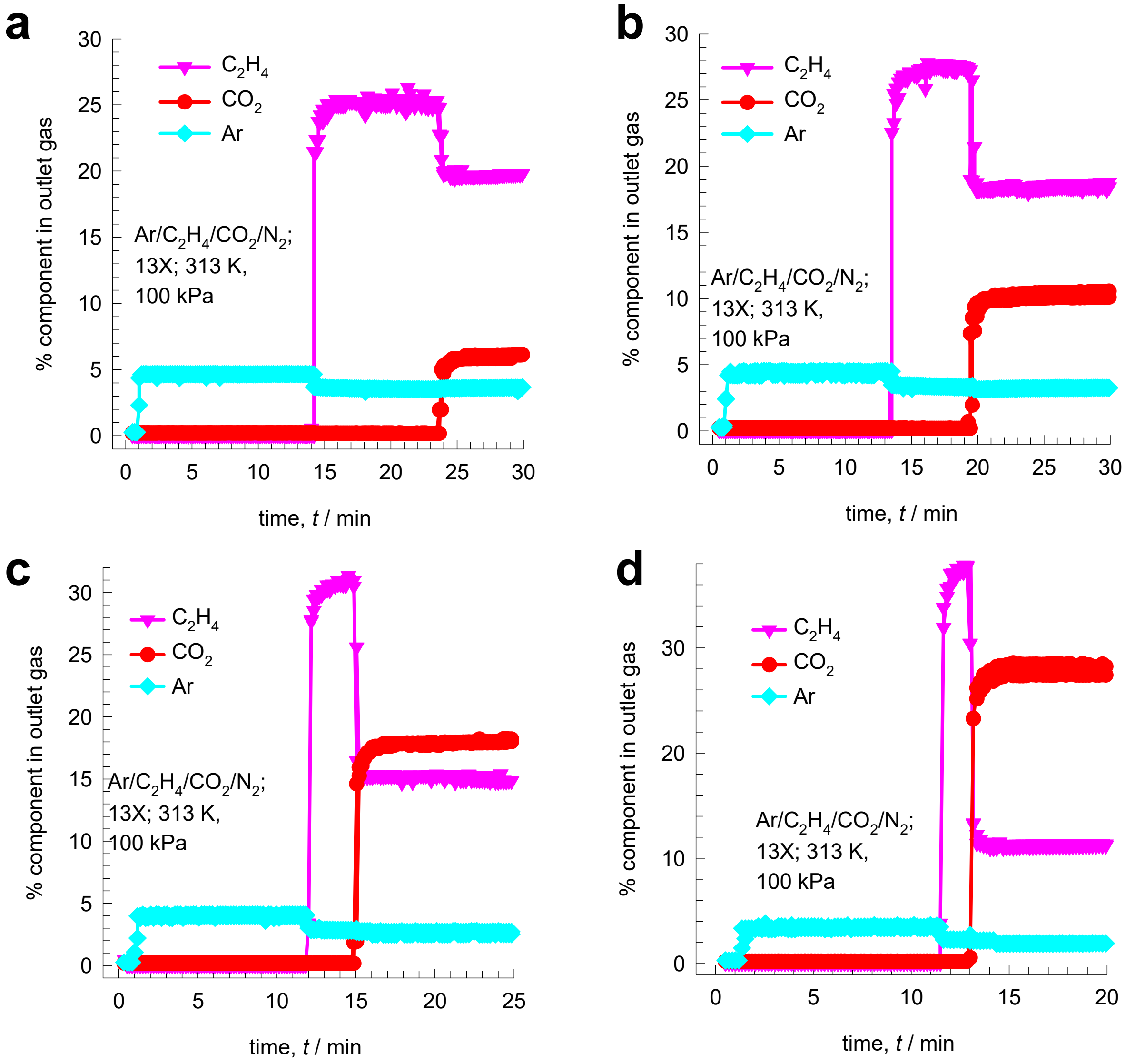

Figure S6. Experimental breakthroughs for Ar/C_2H_4/CO_2/N_2 mixtures in 13X zeolite at 313 K and total pressure of 1 bar for (a) Run1, (b) Run 2, (c) Run 3, and (d) Run 4. The % N_2 in the outlet gas can be determined by the taking the sum of the mole % = 100.

Transient breakthrough experiments vs simulations

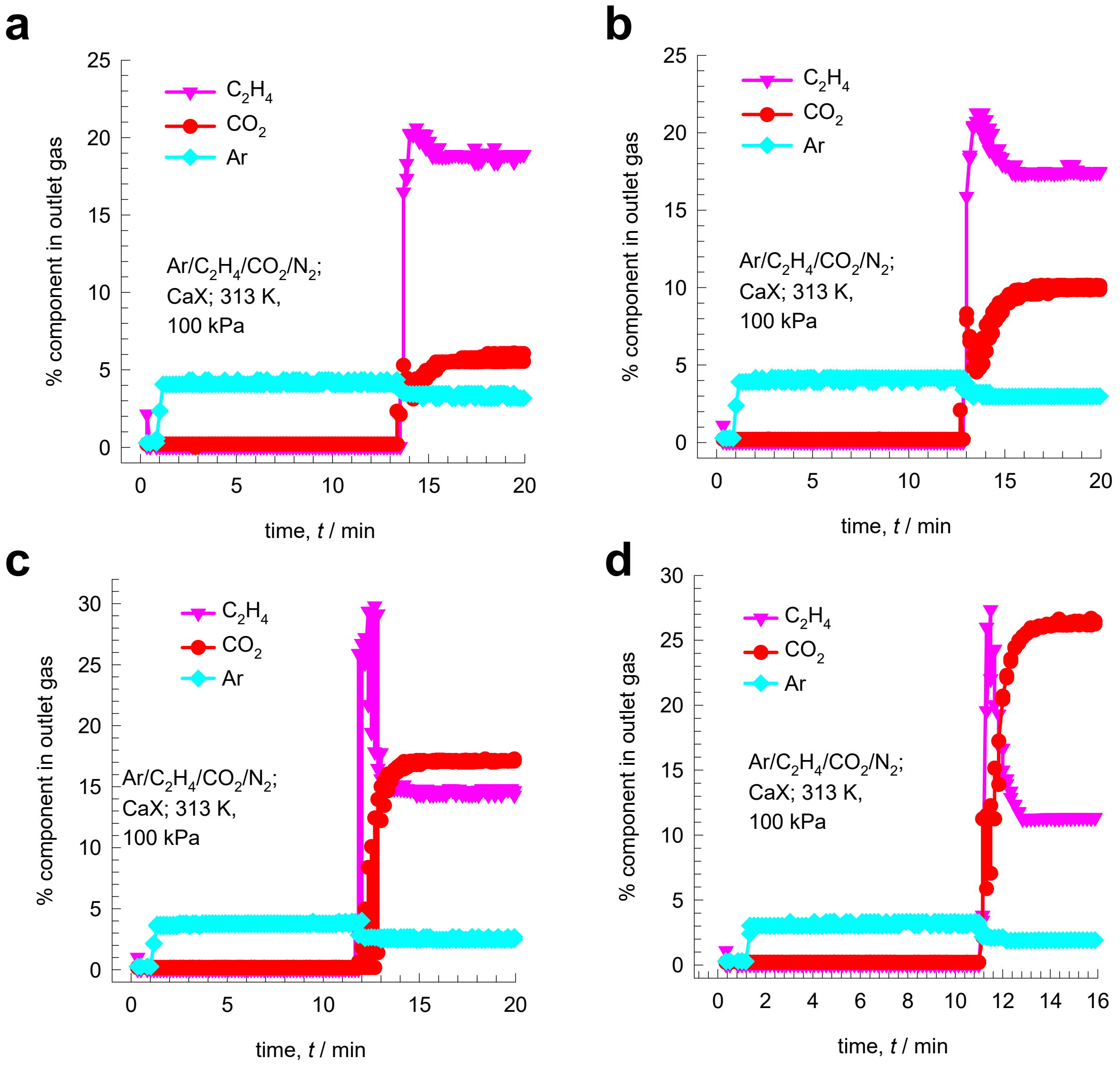

Figure S7. Experimental breakthroughs for $Ar/C_2H_4/CO_2/N_2$ mixtures in CaX zeolite at 313 K and total pressure of 1 bar for (a) Run1, (b) Run 2, (c) Run 3, and (d) Run 4. The % N_2 in the outlet gas can be determined by the taking the sum of the mole % = 100.

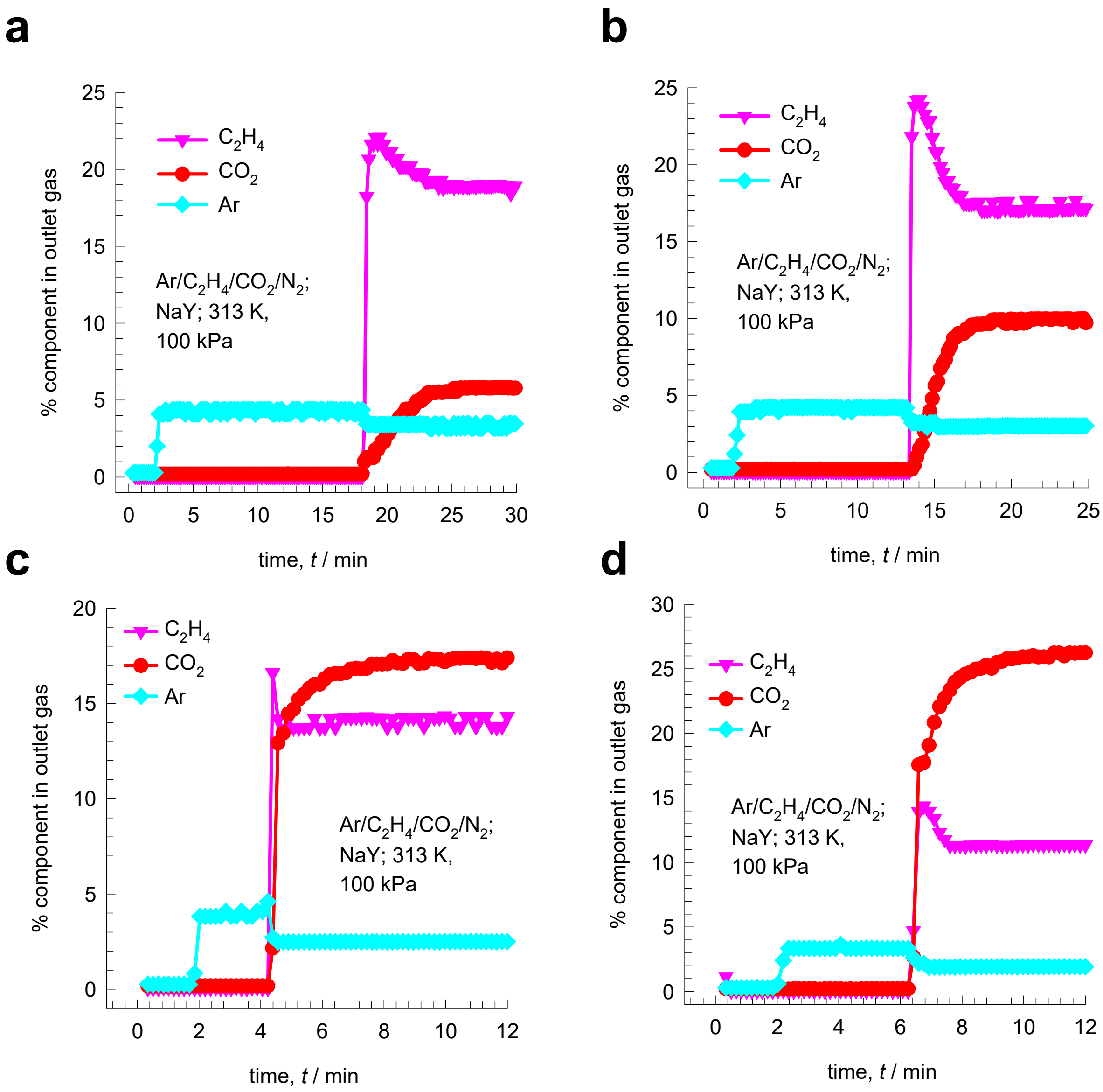

Figure S8. Experimental breakthroughs for Ar/C_2H_4/CO_2/N_2 mixtures in NaY zeolite at 313 K and total pressure of 1 bar for (a) Run1, (b) Run 2, (c) Run 3, and (d) Run 4. The % N_2 in the outlet gas can be determined by the taking the sum of the mole % = 100.

Transient breakthrough experiments vs simulations

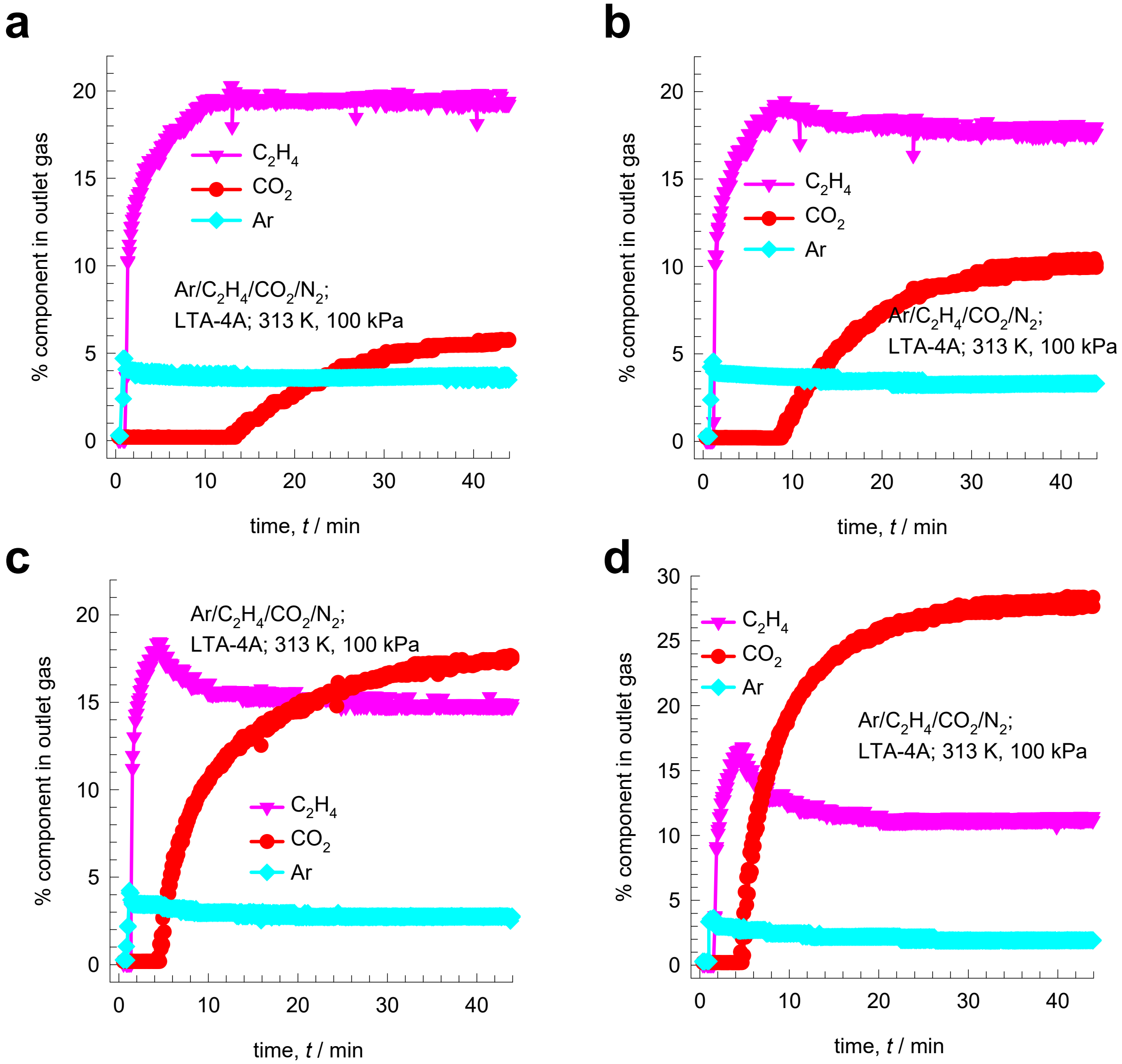

Figure S9. Experimental breakthroughs for Ar/C_2H_4/CO_2/N_2 mixtures in LTA-4A zeolite at 313 K and total pressure of 1 bar for (a) Run1, (b) Run 2, (c) Run 3, and (d) Run 4. The % N_2 in the outlet gas can be determined by the taking the sum of the mole % = 100.

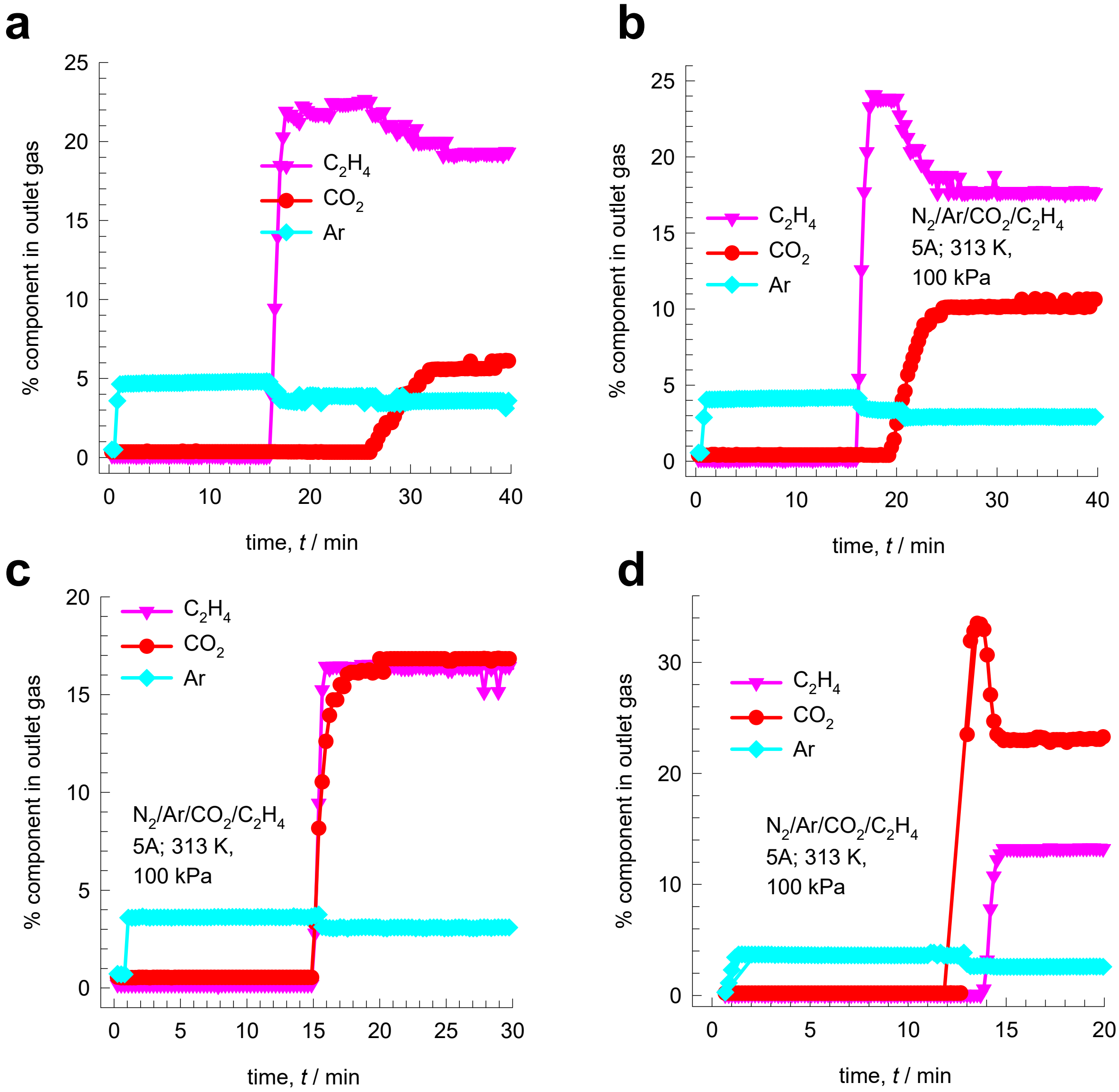

Figure S10. Experimental breakthroughs for $Ar/C_2H_4/CO_2/N_2$ mixtures in LTA-5A zeolite at 313 K and total pressure of 1 bar for (a) Run1, (b) Run 2, (c) Run 3, and (d) Run 4. These data are taken from earlier work.[30] The % N_2 in the outlet gas can be determined by the taking the sum of the mole % = 100.

Transient breakthrough experiments vs simulations

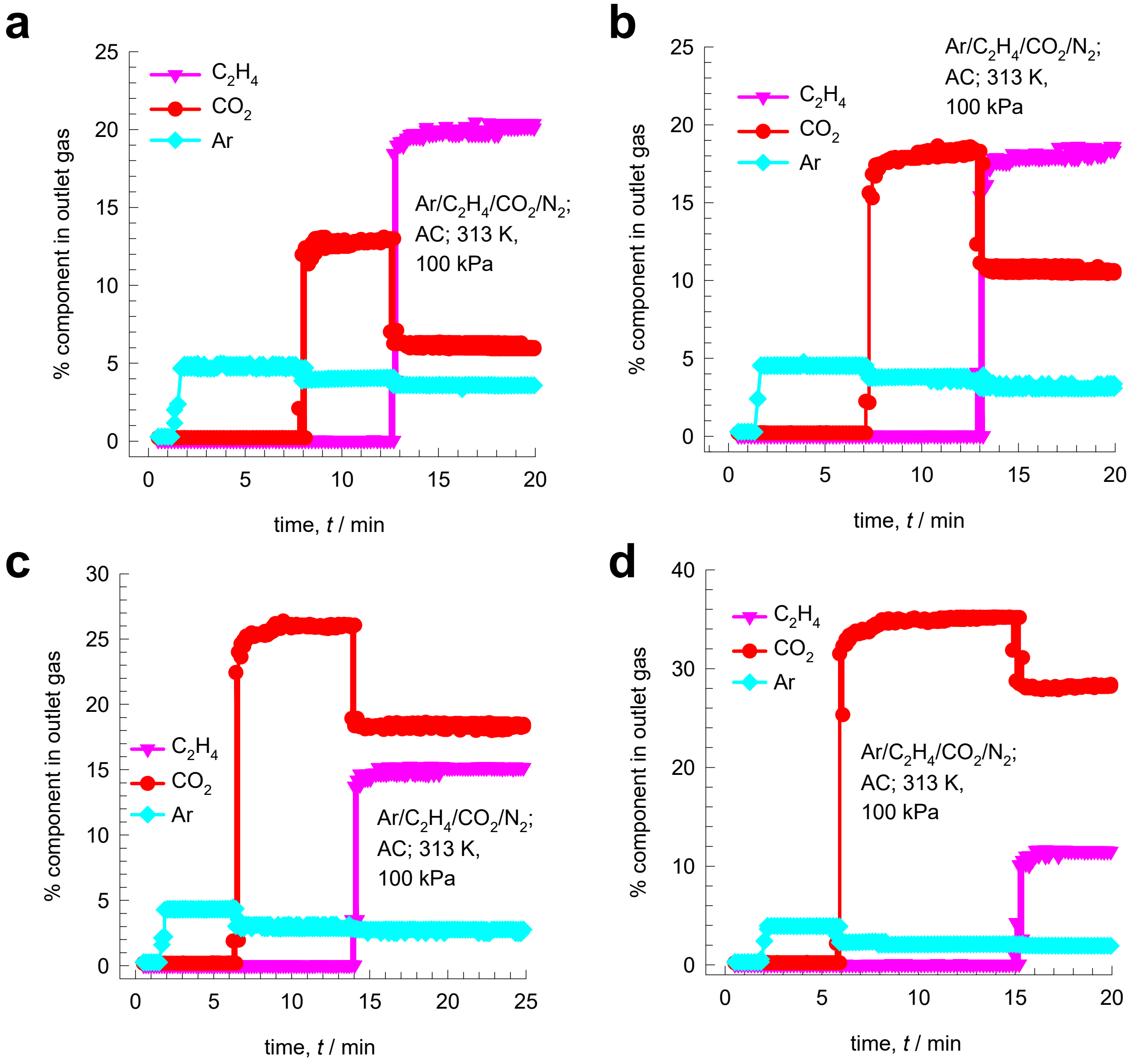

Figure S11. Experimental breakthroughs for Ar/C_2H_4/CO_2/N_2 mixtures in Activated Carbon (AC) at 313 K and total pressure of 1 bar for (a) Run1, (b) Run 2, (c) Run 3, and (d) Run 4. The % N_2 in the outlet gas can be determined by the taking the sum of the mole % = 100.

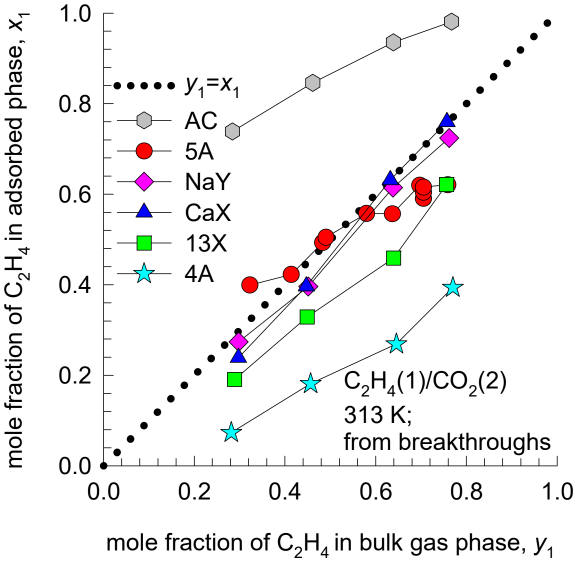

Figure S12. Analysis of the experimental breakthroughs with different sorbents. The adsorbed phase mole fraction of C_2H_4 (*y*-axis) is plotted as a function of the mole fraction of C_2H_4 in the bulk gas phase mixture (*x*-axis). The data for 5A zeolite includes the entire data set obtained at 1 bar and reported in our earlier work.[30]

Transient breakthrough experiments vs simulations

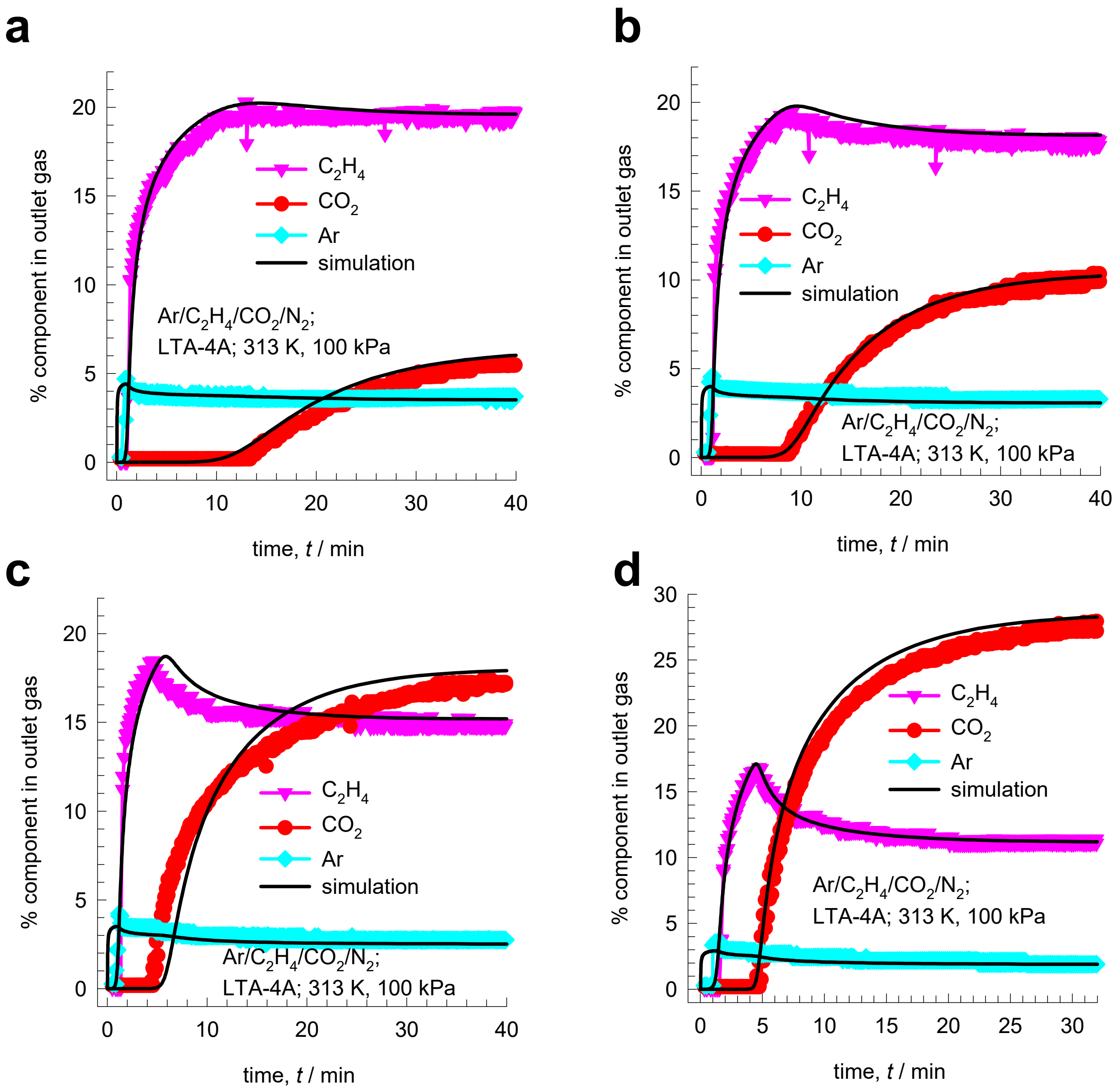

Figure S13. Comparison of transient breakthrough simulations (continuous black solid lines) with experimental breakthroughs for Ar/C_2H_4/CO_2/N_2 mixtures in LTA-4A zeolite at 313 K and total pressure of 1 bar for (a) Run1, (b) Run 2, (c) Run 3, and (d) Run 4. The % N_2 in the outlet gas can be determined by the taking the sum of the mole % = 100.

Transient breakthrough experiments vs simulations

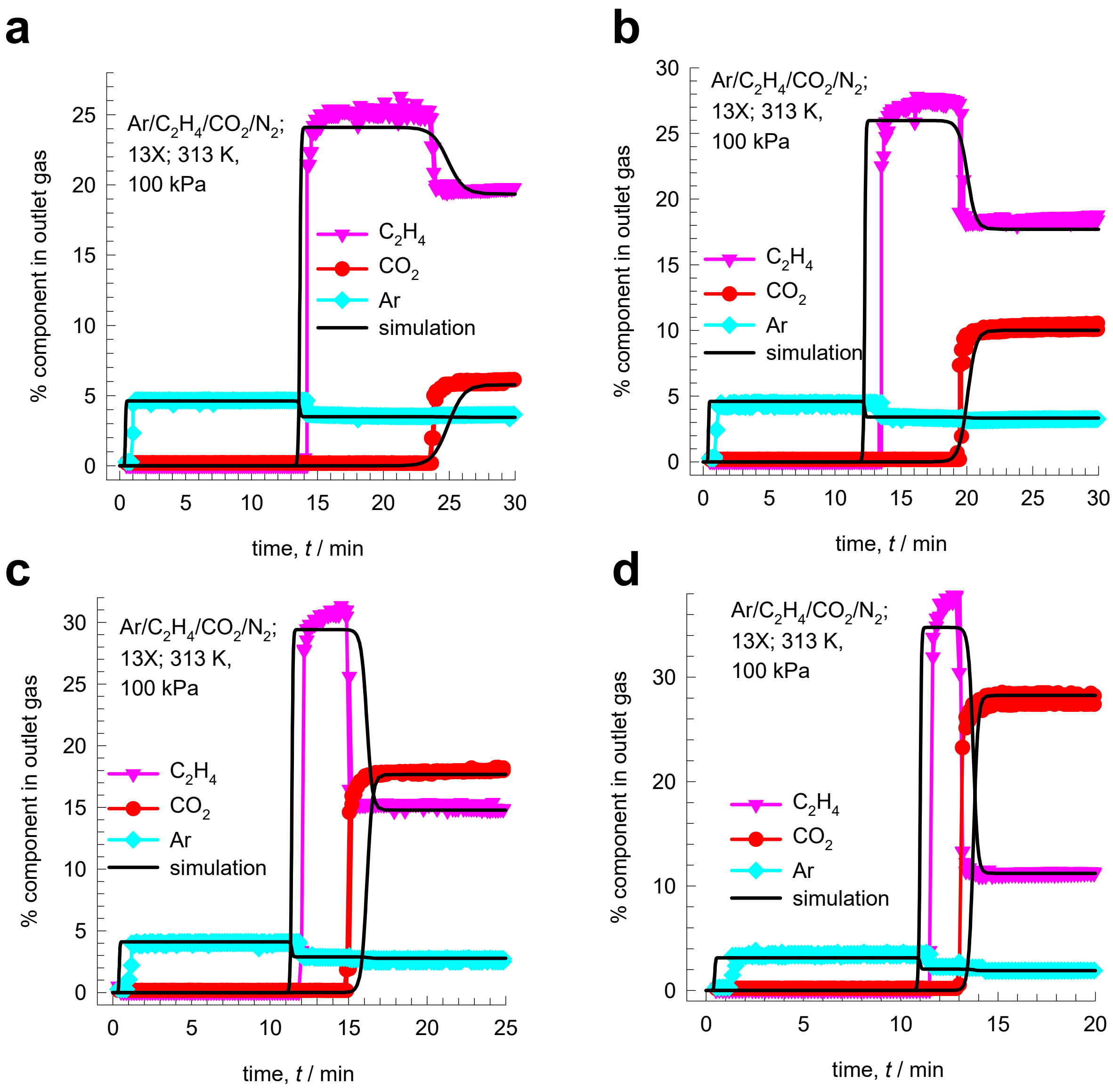

Figure S14. Comparison of transient breakthrough simulations (continuous black solid lines) with experimental breakthroughs for Ar/C_2H_4/CO_2/N_2 mixtures in 13X zeolite at 313 K and total pressure of 1 bar for (a) Run1, (b) Run 2, (c) Run 3, and (d) Run 4. The % N_2 in the outlet gas can be determined by the taking the sum of the mole % = 100.

Transient breakthrough experiments vs simulations

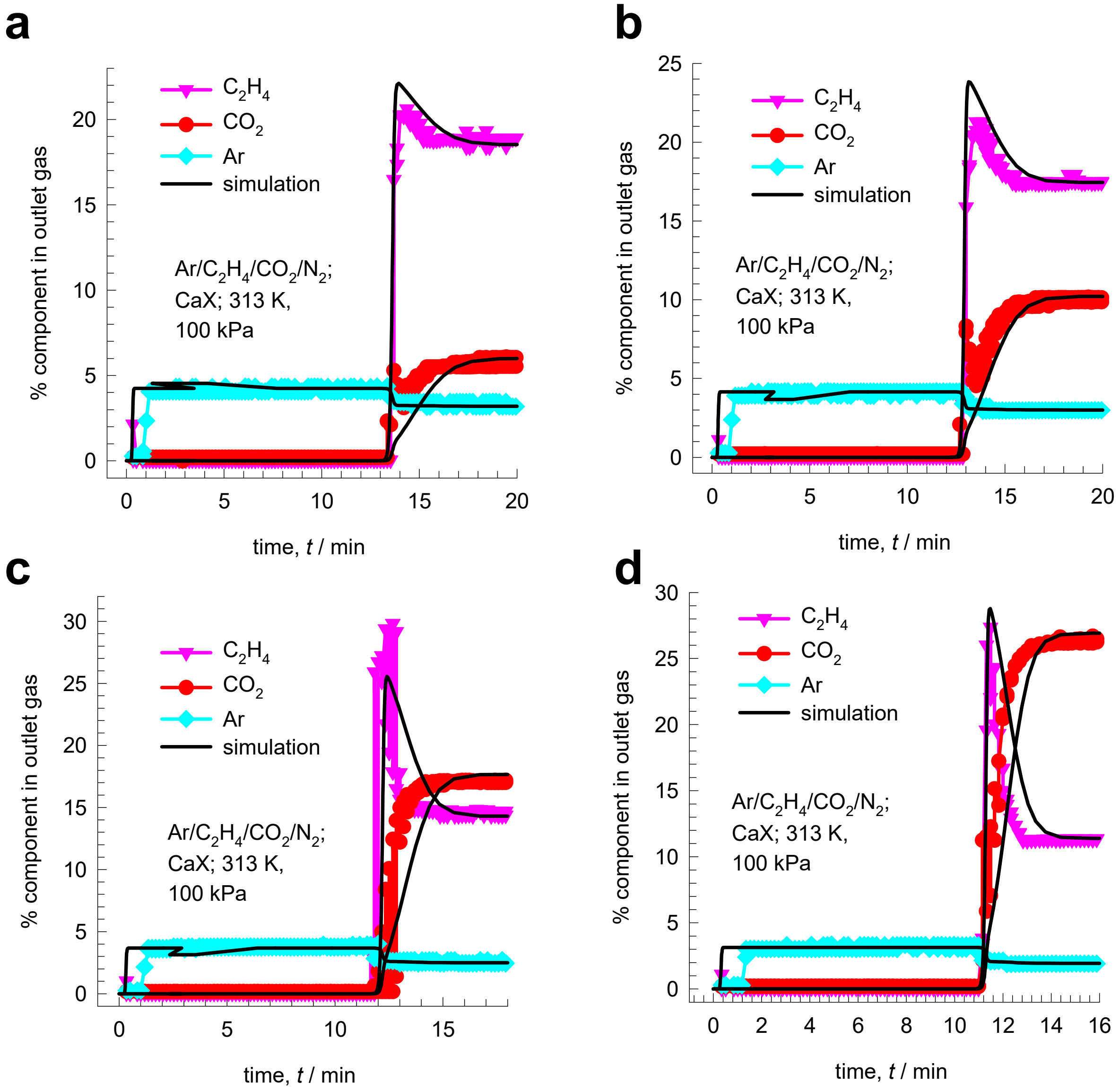

Figure S15. Comparison of transient breakthrough simulations (continuous black solid lines) with experimental breakthroughs for $Ar/C_2H_4/CO_2/N_2$ mixtures in CaX zeolite at 313 K and total pressure of 1 bar for (a) Run1, (b) Run 2, (c) Run 3, and (d) Run 4. The % N_2 in the outlet gas can be determined by the taking the sum of the mole % = 100.

Transient breakthrough experiments vs simulations

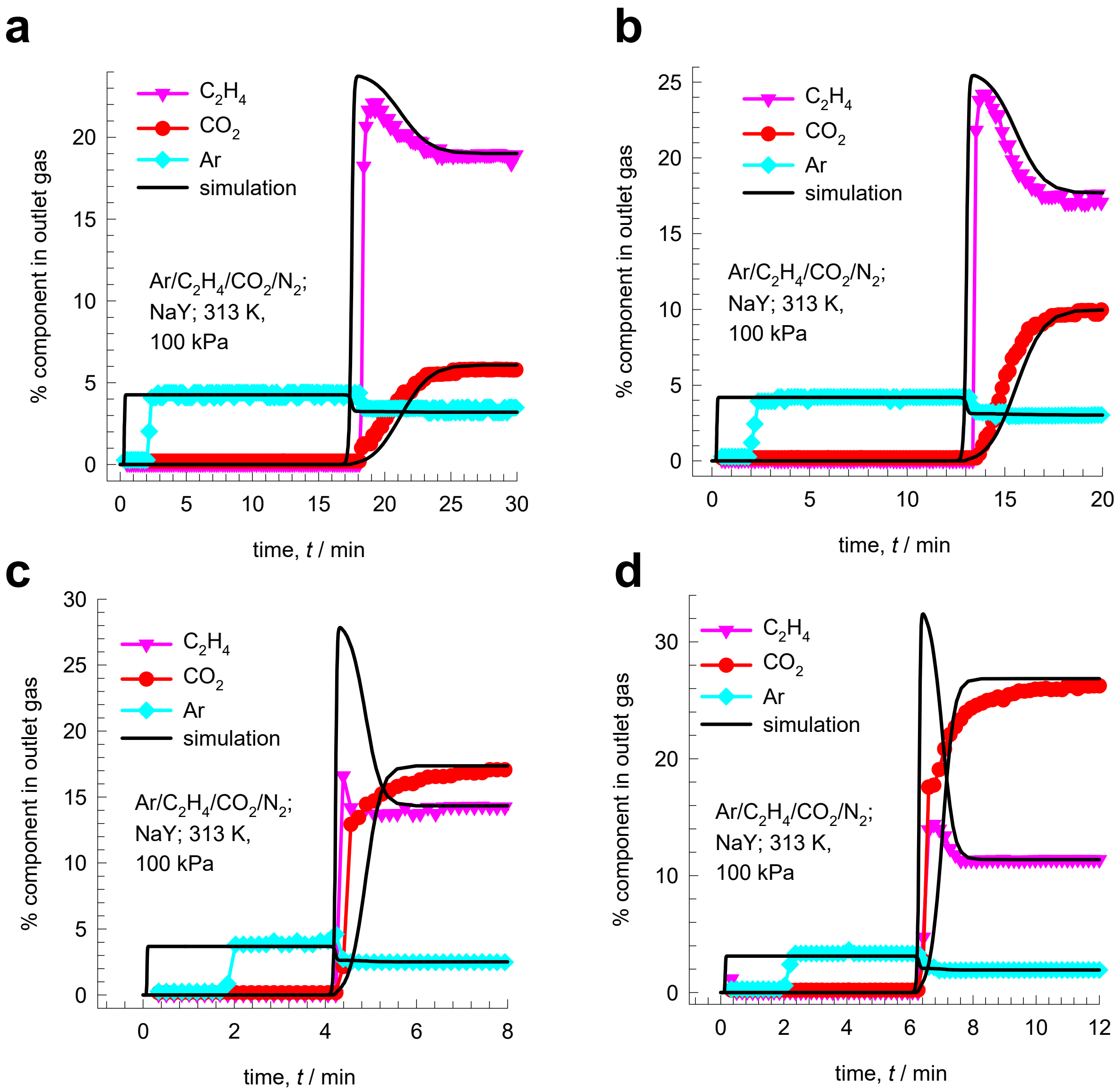

Figure S16. Comparison of transient breakthrough simulations (continuous black solid lines) with experimental breakthroughs for Ar/C_2H_4/CO_2/N_2 mixtures in NaY zeolite at 313 K and total pressure of 1 bar for (a) Run1, (b) Run 2, (c) Run 3, and (d) Run 4. The % N_2 in the outlet gas can be determined by the taking the sum of the mole % = 100.

Transient breakthrough experiments vs simulations

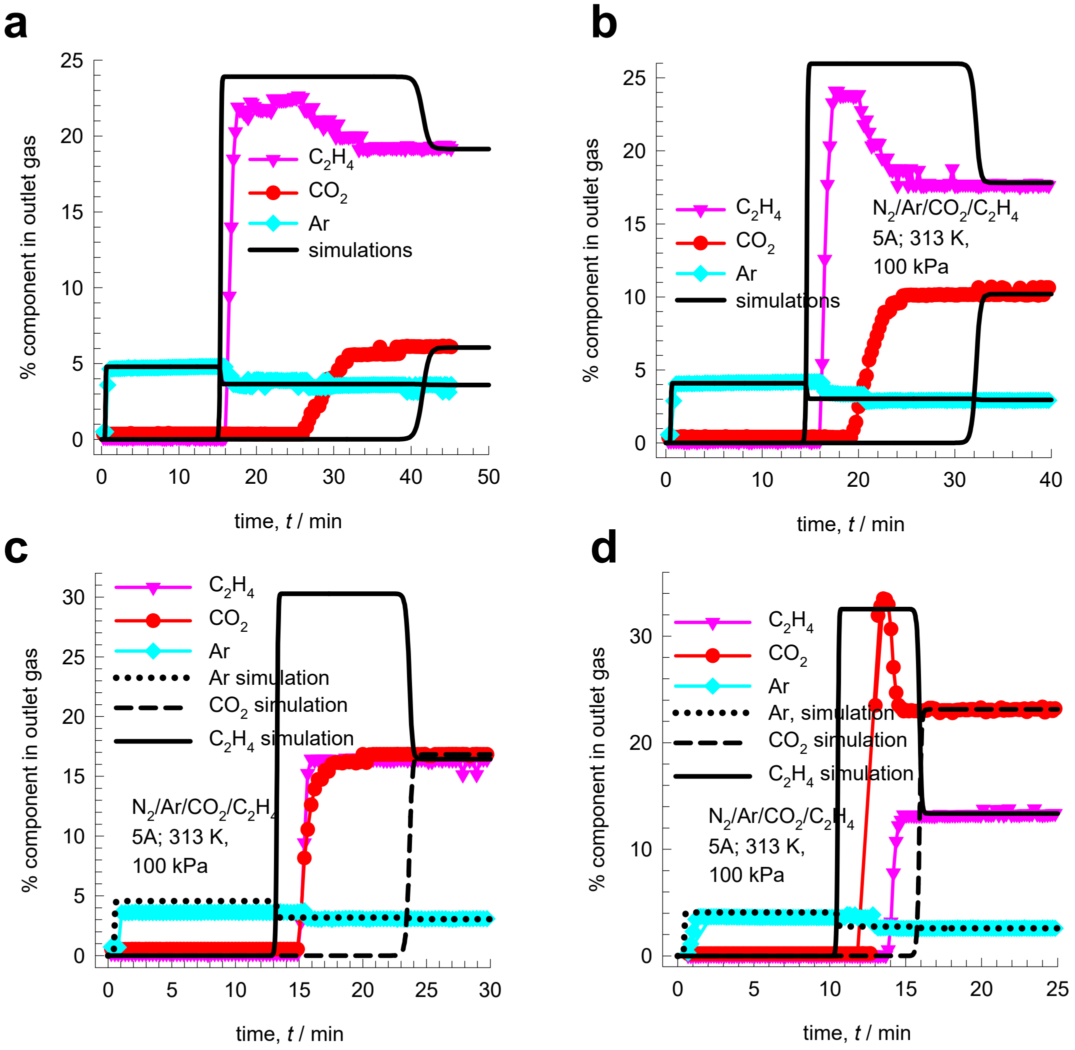

Figure S17. Comparison of transient breakthrough simulations (continuous black solid lines) with experimental breakthroughs for Ar/C_2H_4/CO_2/N_2 mixtures in 5A zeolite at 313 K and total pressure of 1 bar for (a) Run1, (b) Run 2, (c) Run 3, and (d) Run 4. The % N_2 in the outlet gas can be determined by the taking the sum of the mole % = 100.

Transient breakthrough experiments vs simulations

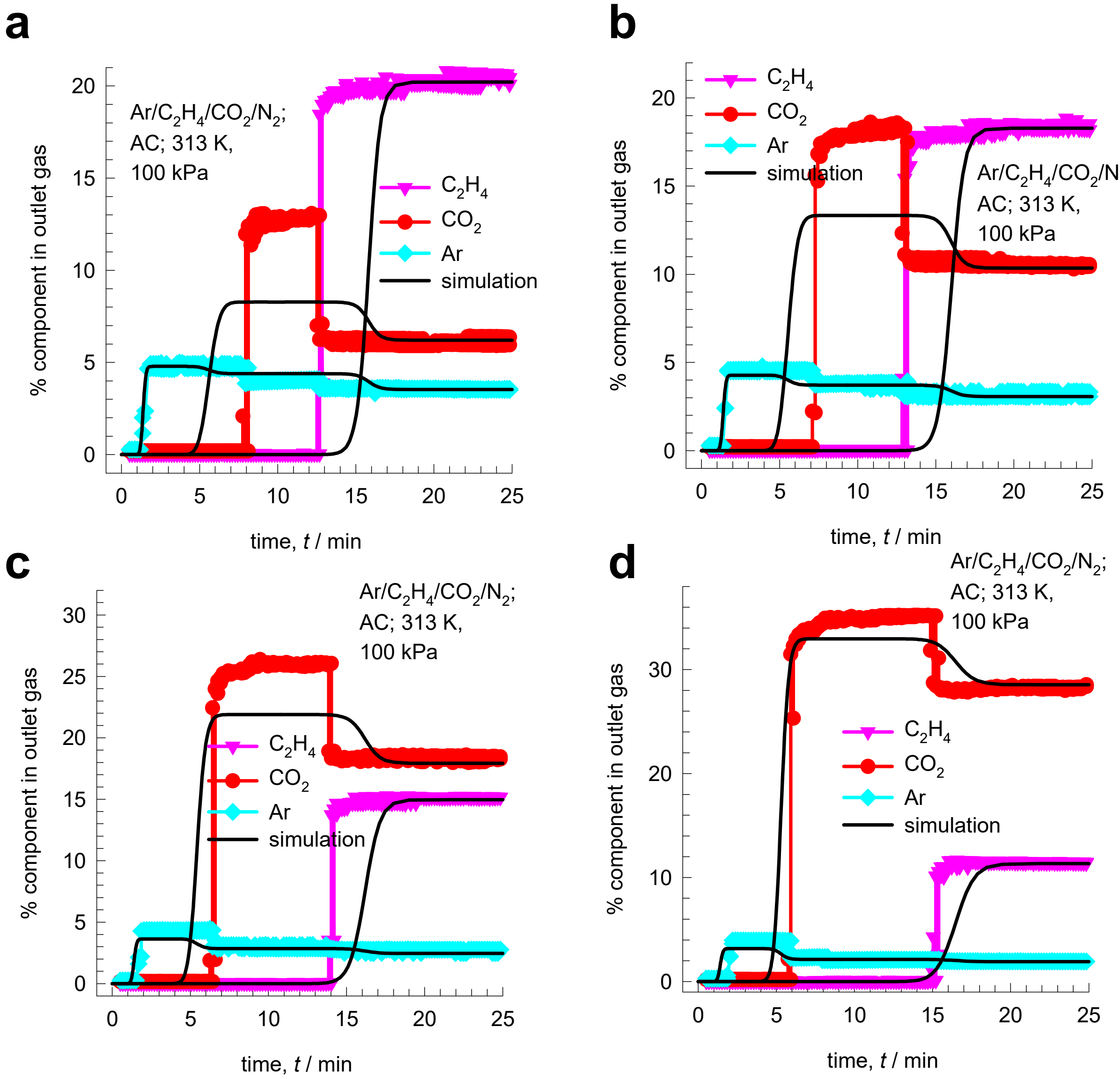

Figure S18. Comparison of transient breakthrough simulations (continuous black solid lines) with experimental breakthroughs for Ar/C$_2$H$_4$/CO$_2$/N$_2$ mixtures in Activated Carbon at 313 K and total pressure of 1 bar for (a) Run1, (b) Run 2, (c) Run 3, and (d) Run 4. The % N$_2$ in the outlet gas can be determined by the taking the sum of the mole % = 100.

7 Non-idealities in C_2H_4/CO_2 mixture adsorption in 5A zeolite

7.1 Analysis of Calleja data for C_2H_4/CO_2 mixture adsorption in 5A zeolite

The paper by Calleja et al.[31] presents evidence of strong non-idealities for adsorption of $C_2H_4(1)/CO_2(2)$ mixtures in LTA-5A zeolite. Their experimental data, obtained at 293 K and total pressure of 10 bar as presented in Figure 3 of their paper has been redrawn for further analysis and discussion in Figure S19.

The Calleja et al.[31] data clearly demonstrate the phenomenon of azeotropic adsorption, $y_1 = x_1; \quad y_2 = x_2$, and selectivity reversals at $y_1 < 0.4$. The experimental data are well represented by the Real Adsorbed Solution Theory (RAST) with the choice of the Wilson parameters $\Lambda_{12} = 35; \quad \Lambda_{21} = 0.75; \quad C = 0.5 \text{ mol kg}^{-1}$.

7.2 Analysis of Basmadjian and Hsieh data for C_2H_4/CO_2 mixture adsorption in 5A zeolite

The paper by Basmadjian and Hsieh[32] presents further evidence of strong non-idealities for adsorption of $C_2H_4(1)/CO_2(2)$ mixtures in LTA-5A zeolite. Their experimental data, obtained at 238 K, 273 Km and 323 K and total pressure of 1.07 bar as presented in Figure 1 of their paper has been redrawn for further in Figure S20a,b,c.

The experimental data at 238 K, showing selectivity reversal at $y_1 < 0.3$, are well described by the Real Adsorbed Solution Theory (RAST) with the choice of the Wilson parameters $\Lambda_{12} = 125; \quad \Lambda_{21} = 2.3; \quad C = 0.07 \text{ mol kg}^{-1}$; see Figure S20a.

The experimental data at 273 K, showing selectivity reversal at $y_1 < 0.35$, are adequately described by the Real Adsorbed Solution Theory (RAST) with the choice of the Wilson parameters $\Lambda_{12} = 60; \quad \Lambda_{21} = 0.067; \quad C = 0.5 \text{ mol kg}^{-1}$; see Figure S20b.

The experimental data at 323 K, showing selectivity reversal at $y_1 < 0.75$, are adequately described by the Real Adsorbed Solution Theory (RAST) with the choice of the Wilson parameters $\Lambda_{12} = 4\times10^{6}; \quad \Lambda_{21} = 10^{-3}; \quad C = 0.013$ mol kg^{-1}; see Figure S20c.

7.3 List of Figures for Non-idealities in C2H4/CO2 mixture adsorption in 5A zeolite

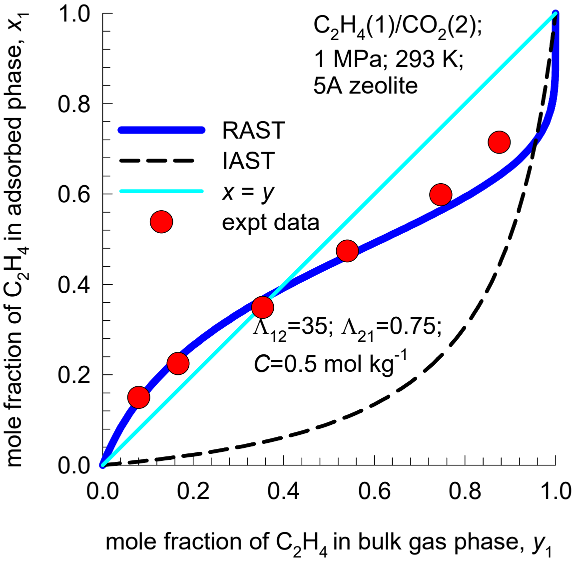

Figure S19. Experimental data of Calleja et al.[31], obtained at 293 K and total pressure of 10 bar, for adsorption of $C_2H_4(1)/CO_2(2)$ mixtures in LTA-5A zeolite. The adsorbed phase mole fraction of C_2H_4, x_1, is plotted as a function of mole fraction of C_2H_4 in the bulk gas phase mixture, y_1. Also indicated at the IAST and RAST calculations of mixture adsorption equilibrium.

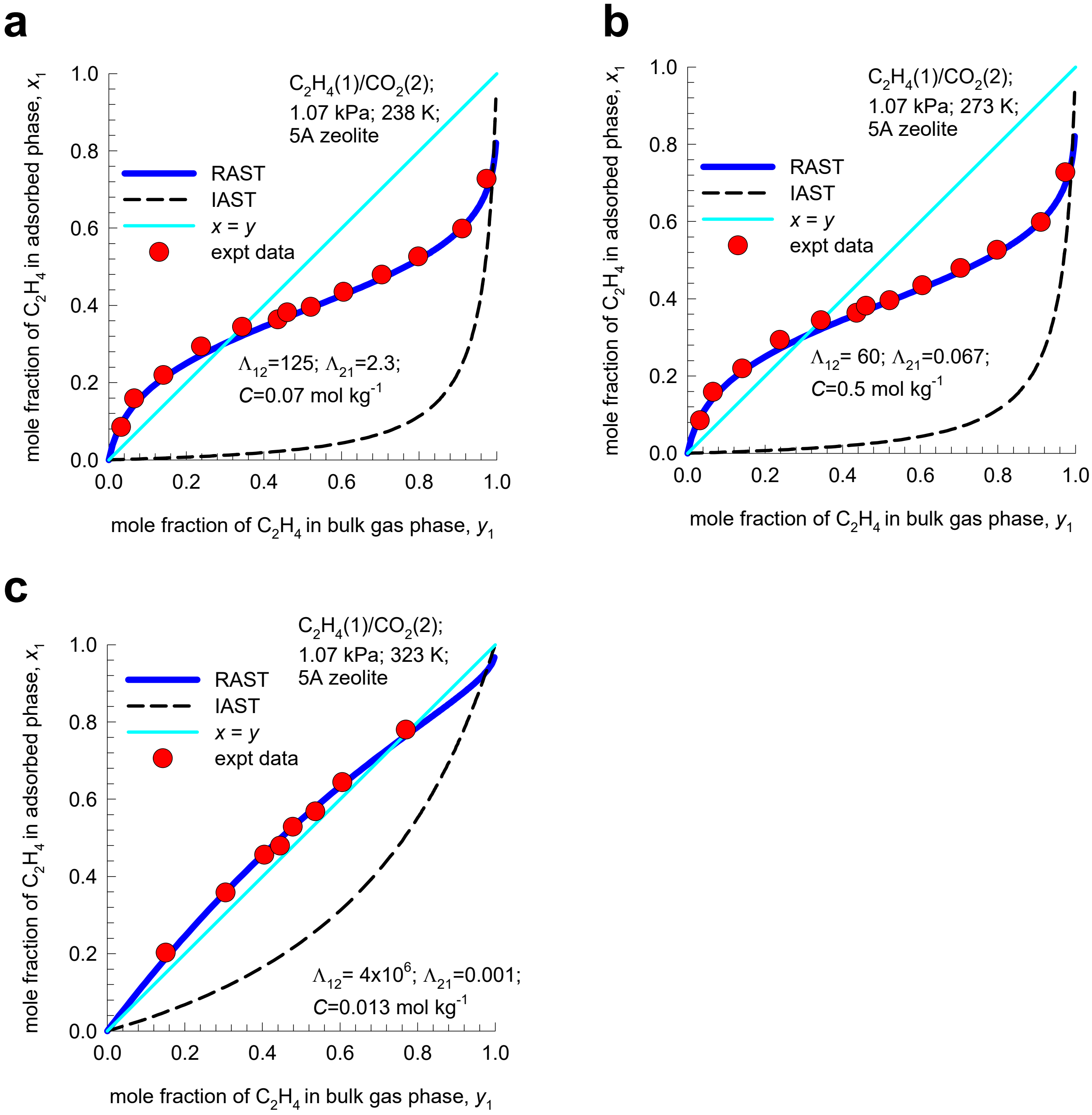

Figure S20. Experimental data of Basmadjian and Hsieh[32], obtained at (a) 238 K, (b) 273 K and (c) 323 K and total pressure of 1.07 bar, for adsorption of $C_2H_4(1)/CO_2(2)$ mixtures in LTA-5A zeolite. The adsorbed phase mole fraction of C_2H_4, x_1, is plotted as a function of mole fraction of C_2H_4 in the bulk gas phase mixture, y_1. Also indicated at the IAST and RAST calculations of mixture adsorption equilibrium.

8 Transient desorption: experiments vs simulations

For each of the Runs 1, 2, 3, and 4 the equilibrated beds for the six sorbents (presented earlier in Figure S6 (13X), Figure S7 (CaX), Figure S8 (NaY) , Figure S9 (LTA-4A), Figure S10 (LTA-5A), and Figure S11 (AC)) were desorption by flow of pure N_2. See also the schematic in Figure S5. The experimental data for % components in the outlet gas, determined by GC/MS are shown (symbols), respectively for the six sorbents, in Figure S21, Figure S22, Figure S23, Figure S24, Figure S25, and Figure S26.

8.1 List of Figures for Transient desorption: experiments vs simulations

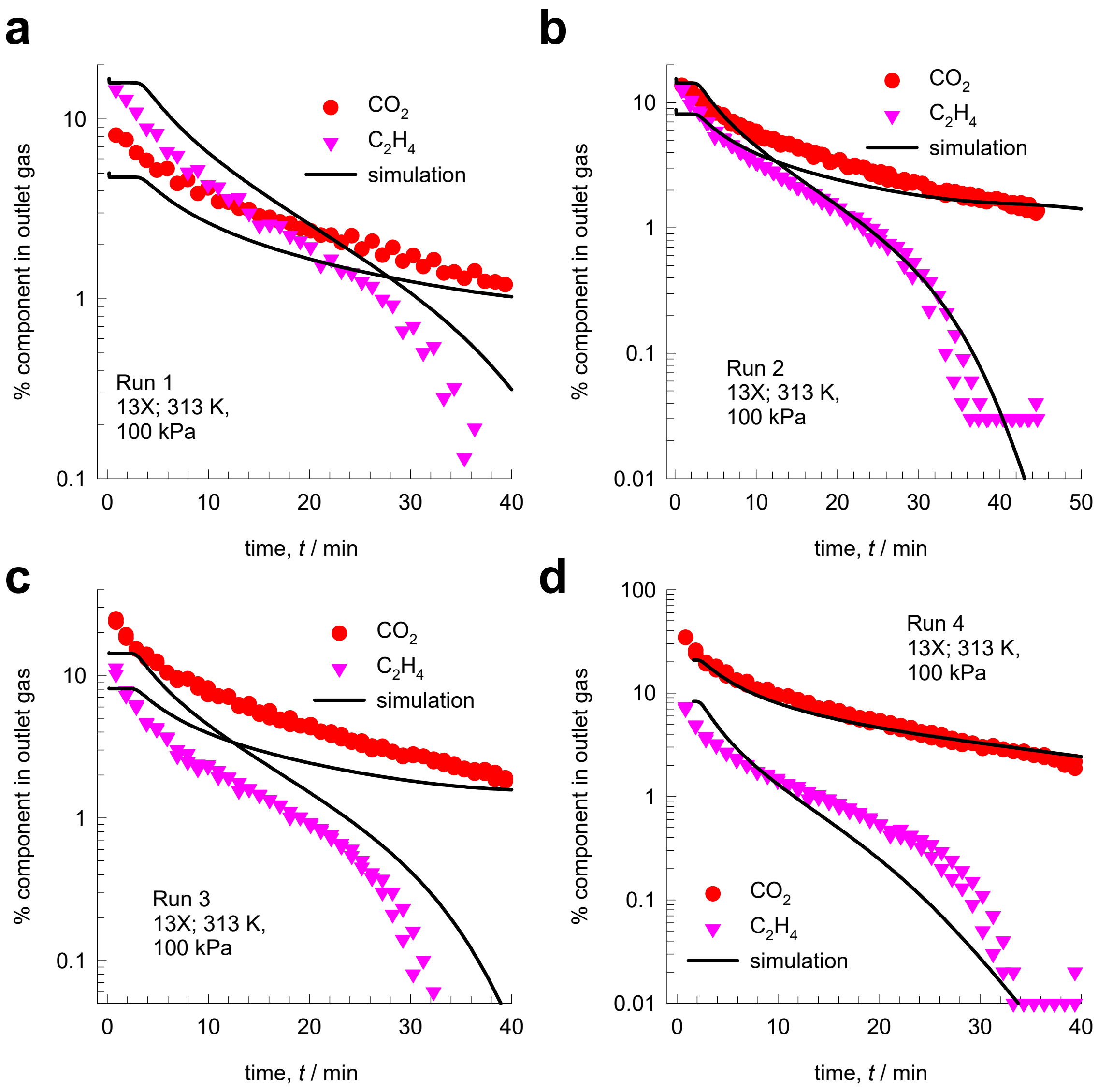

Figure S21. Comparison of transient desorption simulations (continuous black solid lines) with experimental data for desorption of equilibrated 13X zeolite beds for (a) Run1, (b) Run 2, (c) Run 3, and (d) Run 4. The % N_2 in the outlet gas can be determined by the taking the sum of the mole % = 100.

Transient desorption: experiments vs simulations

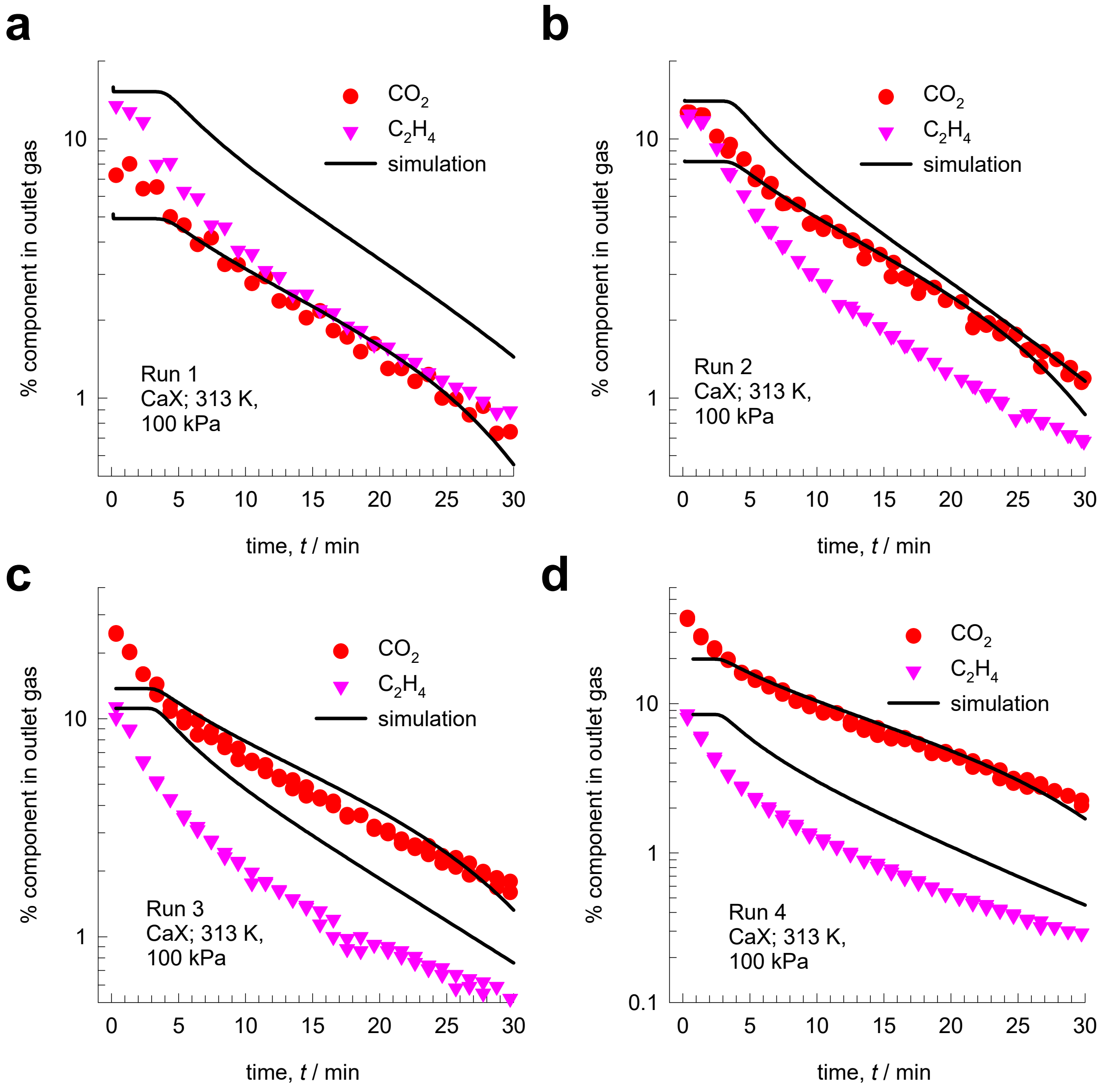

Figure S22. Comparison of transient desorption simulations (continuous black solid lines) with experimental data for desorption of equilibrated CaX zeolite beds for (a) Run1, (b) Run 2, (c) Run 3, and (d) Run 4. The % N_2 in the outlet gas can be determined by the taking the sum of the mole % = 100.

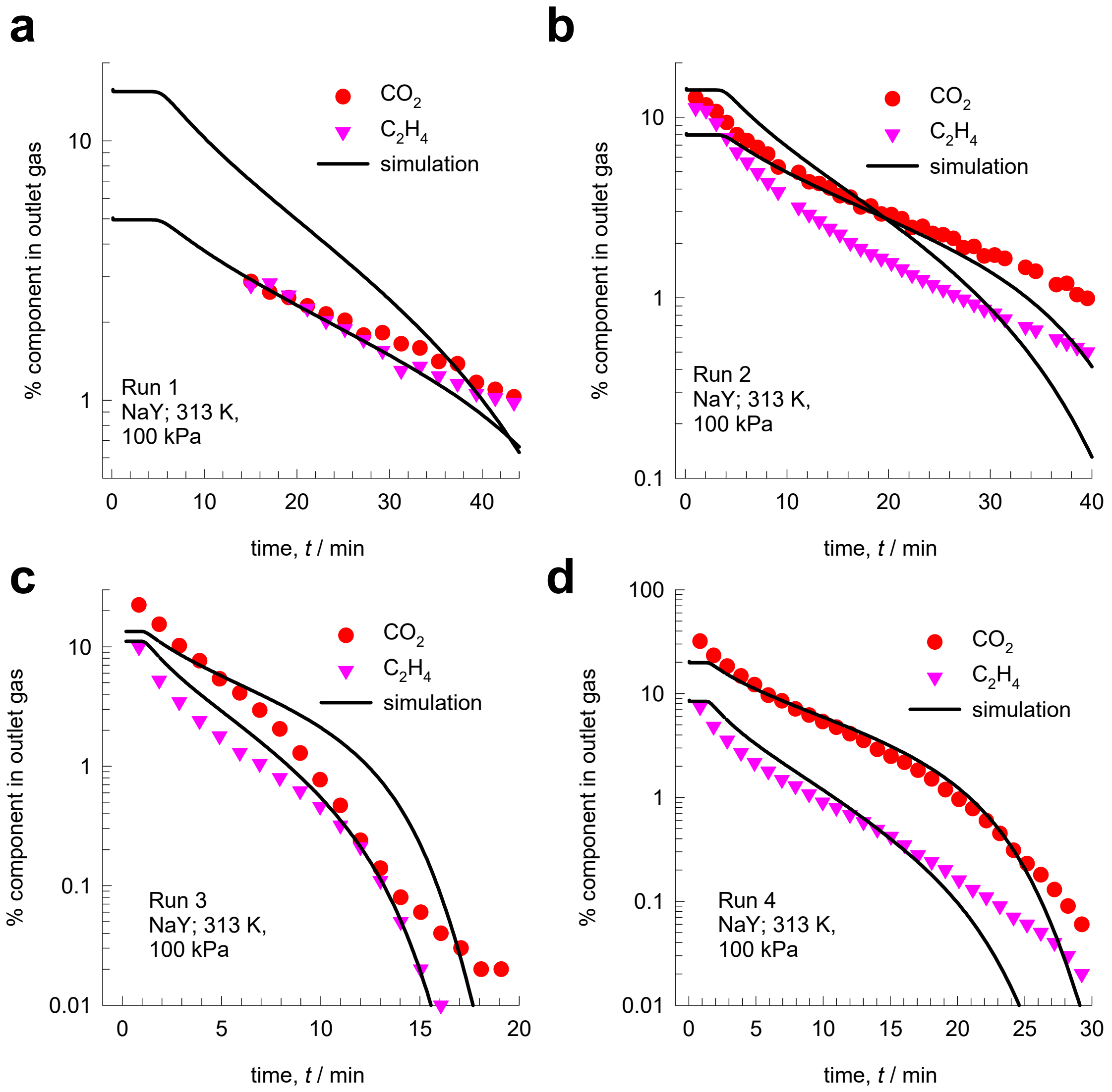

Figure S23. Comparison of transient desorption simulations (continuous black solid lines) with experimental data for desorption of equilibrated NaY zeolite beds for (a) Run1, (b) Run 2, (c) Run 3, and (d) Run 4. The % N_2 in the outlet gas can be determined by the taking the sum of the mole % = 100.

Transient desorption: experiments vs simulations

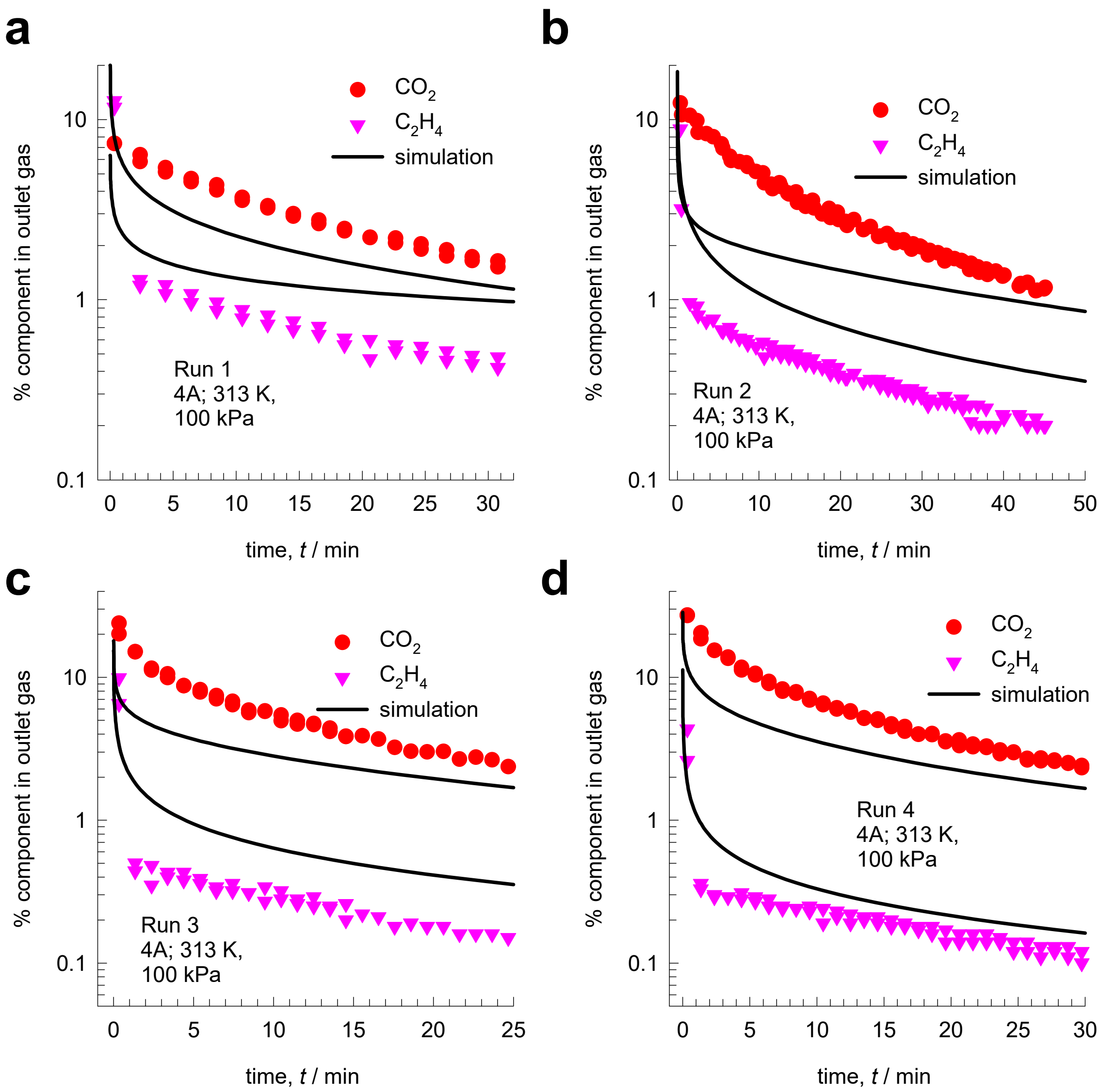

Figure S24. Comparison of transient desorption simulations (continuous black solid lines) with experimental data for desorption of equilibrated 5A zeolite beds for (a) Run1, (b) Run 2, (c) Run 3, and (d) Run 4. The % N_2 in the outlet gas can be determined by the taking the sum of the mole % = 100.

Transient desorption: experiments vs simulations

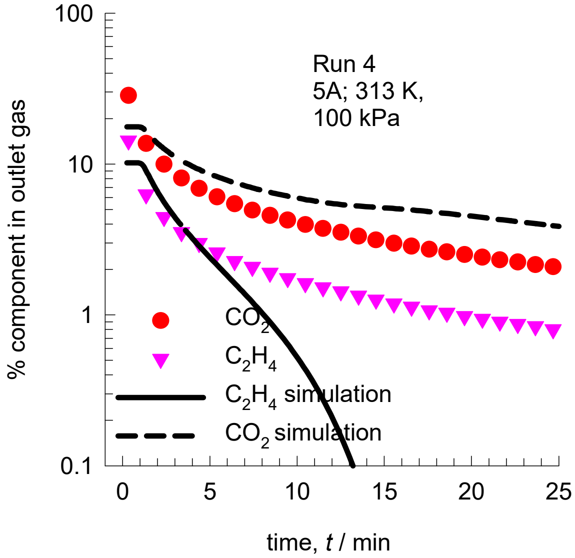

Figure S25. Comparison of transient desorption simulations (continuous black solid lines) with experimental data for desorption of equilibrated 5A zeolite beds for Run 4. The % N_2 in the outlet gas can be determined by the taking the sum of the mole % = 100.

Transient desorption: experiments vs simulations

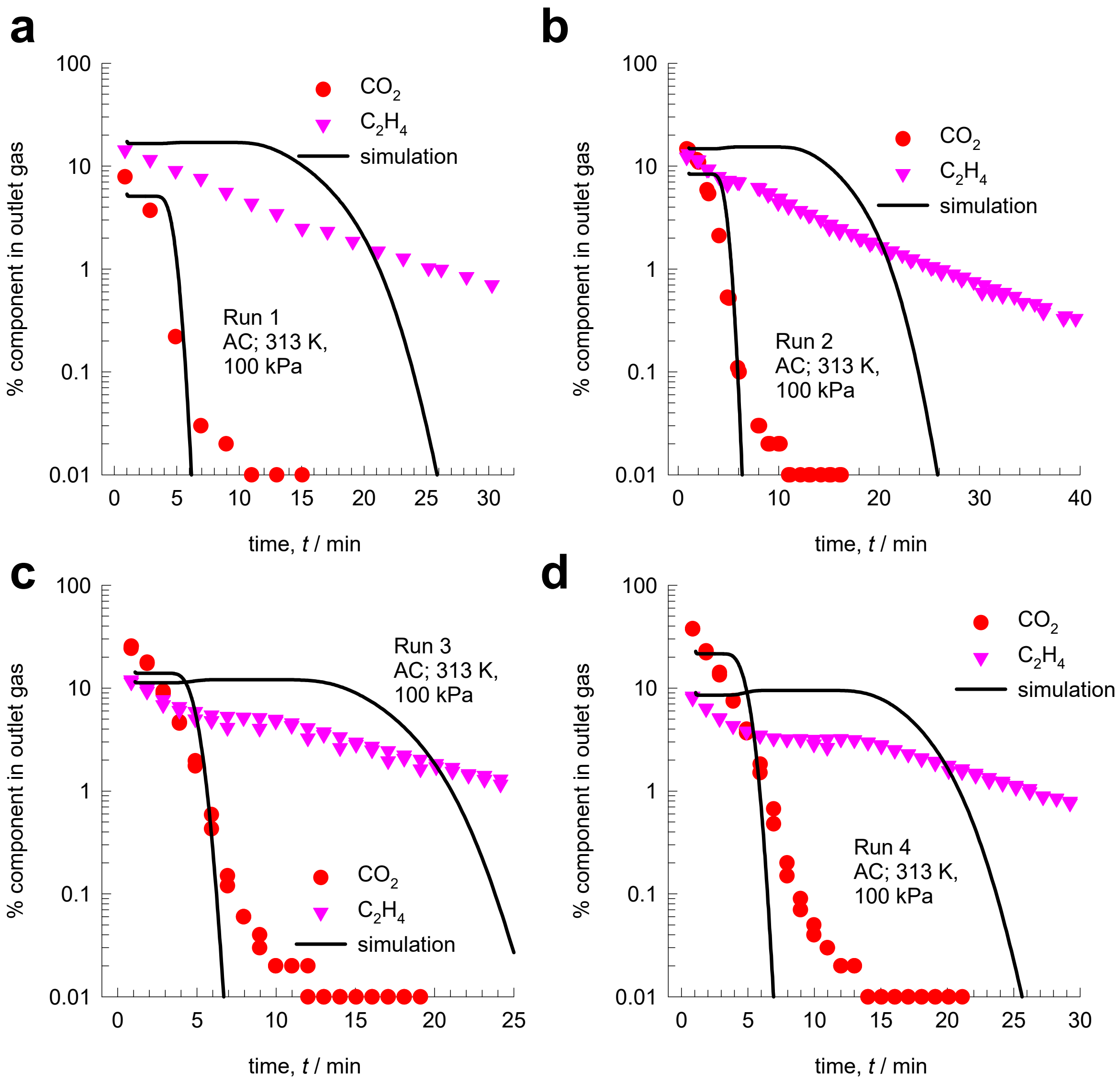

Figure S26. Comparison of transient desorption simulations (continuous black solid lines) with experimental data for desorption of equilibrated AC beds for (a) Run1, (b) Run 2, (c) Run 3, and (d) Run 4. The % N_2 in the outlet gas can be determined by the taking the sum of the mole % = 100.

9 Nomenclature

Latin alphabet

A	surface area per kg of framework, $\mathrm{m^2\ kg^{-1}}$
b_{i}	Langmuir parameter, Pa^{-1}
c_{i}	molar concentration of species *i*, $\mathrm{mol\ m^{-3}}$
c_{t}	total molar concentration in mixture, $\mathrm{mol\ m^{-3}}$
c_{i0}	molar concentration of species *i* in fluid mixture at inlet to adsorber, $\mathrm{mol\ m^{-3}}$
C	constant used in Equation (S18), $\mathrm{kg\ mol^{-1}}$
Đ_{i}	M-S diffusivity of component *i* for molecule-pore interactions, $\mathrm{m^2\ s^{-1}}$
Đ_{ax}	axial dispersion coefficient, $\mathrm{m^2\ s^{-1}}$
E	energy parameter, $\mathrm{J\ mol^{-1}}$
G^{excess}	excess Gibbs free energy, $\mathrm{J\ mol^{-1}}$
L	length of packed bed adsorber, m
n	number of species in the mixture, dimensionless
p_{i}	partial pressure of species *i*, Pa
p_{t}	total system pressure, Pa
P_i^0	sorption pressure, Pa
q_{A}	molar loading species A, $\mathrm{mol\ kg^{-1}}$
$q_{\mathrm{i,sat}}$	molar loading of species *i* at saturation, $\mathrm{mol\ kg^{-1}}$
q_{t}	total molar loading of mixture, $\mathrm{mol\ kg^{-1}}$
r	radial coordinate, m
r_{c}	radius of crystallite, m
R	gas constant, 8.314 $\mathrm{J\ mol^{-1}\ K^{-1}}$

Nomenclature

S_{ads}	adsorption selectivity, dimensionless
t	time, s
T	absolute temperature, K
u	superficial gas velocity in packed bed, m s^{-1}
v	interstitial gas velocity in packed bed, m s^{-1}
V_{p}	pore volume, m^3 kg^{-1}
x_{i}	mole fraction of species *i* in adsorbed phase, dimensionless
y_{i}	mole fraction of species *i* in bulk fluid mixture, dimensionless
z	distance along the adsorber, and along membrane layer, m

Greek letters

γ_{i}	activity coefficient of component *i* in adsorbed phase, dimensionless
ε	voidage of packed bed, dimensionless
Λ_{ij}	Wilson parameters, dimensionless
μ_{i}	molar chemical potential, J mol^{-1}
π	spreading pressure, N m^{-1}
ρ	framework density, kg m^{-3}
τ	time, dimensionless

Subscripts

i,j	components in mixture
i	referring to component *i*
t	referring to total mixture
sat	referring to saturation conditions

Nomenclature

Superscripts

0	referring to pure component loading
excess	referring to excess parameter

10 References

(1) Mofarahi, M.; Salehi, S. M. Pure and Binary Adsorption Isotherms of Ethylene and Ethane on Zeolite 5A. *Adsorption* **2013**, *19*, 101-110.

(2) Mofarahi, M.; Gholipour, F. Gas Adsorption Separation of CO_2/CH_4 System using Zeolite 5A. *Microporous Mesoporous Mater.* **2014**, *200*, 47-54.

(3) Bakhtyari, A.; Mofarahi, M. Pure and Binary Adsorption Equilibria of Methane and Nitrogen on Zeolite 5A. *J. Chem. Eng. Data* **2014**, *59*, 626-639.

(4) Costa, E.; Calleja, G.; Jimenez, A.; Pau, J. Adsorption Equilibrium of Ethylene, Propane, Propylene, Carbon Dioxide, and Their Mixtures in 13X Zeolite. *J. Chem. Eng. Data* **1991**, *36*, 218-224.

(5) Cavenati, S.; Grande, C. A.; Rodrigues, A. E. Adsorption Equilibrium of Methane, Carbon Dioxide, and Nitrogen on Zeolite 13X at High Pressures. *J. Chem. Eng. Data* **2004**, *49*, 1095-1101.

(6) Bachman, J. E.; Reed, D. A.; Kapelewski, M. T.; Chachra, G.; Jonnavittula, D.; Radaelli, G.; Long, J. R. Enabling alternative ethylene production through its selective adsorption in the metal–organic framework Mn_2(*m*-dobdc). *Energy Environ. Sci.* **2018**, *11*, 2423-2431. http://dx.doi.org/doi:10.1039/c8ee01332b.

(7) Choudhary, V. R.; Mayadevi, S.; Singh, A. P. Sorption Isotherms of Methane, Ethane, Ethene and Carbon Dioxide on NaX, NaY and Na-mordenite Zeolites. *J. Chem. Soc. Faraday Trans.* **1995**, *91*, 2935-2944.

(8) Romero-Pérez, A.; Aguilar-Armenta, G. Adsorption Kinetics and Equilibria of Carbon Dioxide, Ethylene, and Ethane on 4A(CECA) Zeolite. *J. Chem. Eng. Data* **2010**, *55*, 3625-3630.

(9) Reich, R.; Zlegler, W. T.; Rogers, K. A. Adsorption of Methane, Ethane, and Ethylene Gases and Their Binary and Ternary Mixtures and Carbon Dioxide on Activated Carbon at 212-301 K and Pressures to 35 Atmospheres. *Ind. Eng. Chem. Process Des. Dev.* **1980**, *19*, 336-344.

(10) Park, Y.; Moon, D.-K.; Kim, Y.-H.; Ahn, H.; Lee, C.-H. Adsorption isotherms of CO_2, CO, N_2, CH_4, Ar and H_2 on activated carbon and zeolite LiX up to 1.0 MPa. *Adsorption* **2014**, *20*, 631-647. https://doi.org/10.1007/s10450-014-9608-x.

(11) Ruthven, D. M. *Principles of Adsorption and Adsorption Processes*. John Wiley: New York, 1984.

(12) Myers, A. L.; Prausnitz, J. M. Thermodynamics of Mixed Gas Adsorption. *A.I.Ch.E.J.* **1965**, *11*, 121-130.

(13) Siperstein, F. R.; Myers, A. L. Mixed-Gas Adsorption. *A.I.Ch.E.J.* **2001**, *47*, 1141-1159.

(14) Talu, O.; Myers, A. L. Rigorous Thermodynamic Treatment of Gas-Adsorption. *A.I.Ch.E.J.* **1988**, *34*, 1887-1893.

(15) Talu, O.; Zwiebel, I. Multicomponent Adsorption Equilibria of Nonideal Mixtures. *A.I.Ch.E.J.* **1986**, *32*, 1263-1276.

(16) Krishna, R. Screening Metal-Organic Frameworks for Mixture Separations in Fixed-Bed Adsorbers using a Combined Selectivity/Capacity Metric. *RSC Adv.* **2017**, *7*, 35724-35737. https://doi.org/10.1039/C7RA07363A.

(17) Krishna, R. Methodologies for Evaluation of Metal-Organic Frameworks in Separation Applications. *RSC Adv.* **2015**, *5*, 52269-52295.

References

(18) Krishna, R. The Maxwell-Stefan Description of Mixture Diffusion in Nanoporous Crystalline Materials. *Microporous Mesoporous Mater.* **2014**, *185*, 30-50.

(19) Krishna, R. Tracing the Origins of Transient Overshoots for Binary Mixture Diffusion in Microporous Crystalline Materials. *Phys. Chem. Chem. Phys.* **2016**, *18*, 15482-15495.

(20) Krishna, R.; Baur, R. Modelling Issues in Zeolite Based Separation Processes. *Sep. Purif. Technol.* **2003**, *33*, 213-254.

(21) Krishna, R.; Baur, R. Diffusion, Adsorption and Reaction in Zeolites: Modelling and Numerical Issues. http://krishna.amsterchem.com/zeolite/, University of Amsterdam, Amsterdam, 1 January 2015.

(22) Ruthven, D. M.; Farooq, S.; Knaebel, K. S. *Pressure swing adsorption*. VCH Publishers: New York, 1994.

(23) Kooijman, H. A.; Taylor, R. A dynamic nonequilibrium model of tray distillation columns. *A.I.Ch.E.J.* **1995**, *41*, 1852-1863.

(24) Michelsen, M. An efficient general purpose method of integration of stiff ordinary differential equations. *A.I.Ch.E.J.* **1976**, *22*, 594-597.

(25) Bulirsch, R.; Stoer, J. Numerical treatment of ordinary differential equations by extrapolation methods. *Numer. Math.* **1966**, *8*, 1-14.

(26) Krishna, R.; van Baten, J. M. Investigating the potential of MgMOF-74 membranes for CO_2 capture. *J. Membr. Sci.* **2011**, *377*, 249-260.

(27) He, Y.; Krishna, R.; Chen, B. Metal-Organic Frameworks with Potential for Energy-Efficient Adsorptive Separation of Light Hydrocarbons. *Energy Environ. Sci.* **2012**, *5*, 9107-9120.

(28) van Zandvoort, I.; van Klink, G. P. M.; de Jong, E.; van der Waal, J. C. Selectivity and Stability of Zeolites [Ca]A and [Ag]A towards Ethylene Adsorption and Desorption from Complex Gas Mixtures. *Microporous Mesoporous Mat.* **2018**, *263*, 142-149.

(29) Yu, H.; Wang, X.; Xu, C.; Chen, D.-L.; Zhu, W.; Krishna, R. Utilizing transient breakthroughs for evaluating the potential of Kureha carbon for CO_2 capture. *Chem. Eng. J.* **2015**, *269*, 135-147.

(30) van Zandvoort, I.; van der Waal, J. K.; Ras, E.-J.; de Graaf, R.; Krishna, R. Highlighting non-idealities in C_2H_4/CO_2 mixture adsorption in 5A zeolite. *Sep. Purif. Technol.* **2019**, *227*, 115730. https://doi.org/10.1016/j.seppur.2019.115730.

(31) Calleja G.; Pau J.; Perez P.; J.A., C. *Binary and Ternary Adsorption Equilibria at High Pressure on Molecular Sieves*. Fundamentals of Adsorption FOA 1996; Edited by L. M.D., 147-154, The Kluwer International Series in Engineering and Computer Science: Boston, Massachusetts, 1996.(https://doi.org/10.1007/978-1-4613-1375-5_17)

(32) Basmadjian, D.; Hsieh, S. T. Isothermal Column Sorption of Ethylene-Carbon Dioxide Mixtures with Azeotropic Behaviour. *Can. J. Chem. Eng.* **1980**, *58*, 185-189. https://doi.org/10.1002/cjce.5450580208.